https://doi.org/10.5194/egusphere-2026-2927
Preprint. Discussion started: 31 July 2026

Description and Demonstration of the Multilayer Emission Model "2S L-MEM" for Passive L-Band Satellite Observations on Land

Manu Holmberg[1], Mike Schwank[2,3], Andreas Colliander[1], Juliette Ortet[1], Juha Lemmetyinen[1], Yiwen Zhou[2], Philippe Richaume[4], Cristina Vittucci[5], Kimmo Rautiainen[1], Arnaud Mialon[4], and Yann Kerr[4]

[1]Finnish Meteorological Institute, 00101 Helsinki, Finland
[2]Swiss Federal Institute WSL, Zürcherstrasse 111, 8903 Birmensdorf, Switzerland
[3]GAMMA Remote Sensing Research and Consulting AG, Worbstr. 225, 3073 Gümligen, Switzerland
[4]CESBIO (Université de Toulouse, CNES, CNRS, IRD, INRAE, UPS), 31401 Toulouse, France
[5]University of Rome Tor Vergata, 00133 Rome, Italy

Correspondence: Manu Holmberg (manu.holmberg@fmi.fi)

Abstract. This paper presents and reviews the modeling of satellite-observed L-band brightness temperature (BT) over land using the two-stream multi-layer microwave emission model (2S-MEM). While the 2S-MEM has been applied in several earlier studies, a comprehensive description tailored to the interpretation of satellite based passive L-band observations has been lacking. Here, we consolidate and clarify the different components of the model formulation in the context of satellite-based L-band radiometry and demonstrate its practical application across various scenarios. Three case studies from different in situ sites and corresponding L-band BT datasets from ESA's SMOS and NASA's SMAP satellites are presented. In each case study, BTs are simulated from in situ measurements and compared with corresponding satellite observations. We discuss the challenges of modeling coarse-resolution L-band BTs measured by satellite using in situ point data, and the resulting uncertainties in BT simulations that must be considered in both forward and inverse applications, including geophysical parameter retrievals.

1 Introduction

For more than a decade, operational satellite missions have provided a continuous stream of passive microwave observations at L-band ($1-2$ GHz). These missions measure the thermal emission of Earth surface at this low microwave frequency, expressed in brightness temperatures (BTs), providing a unique source of information for retrieving numerous essential climate variables (ECVs) (Bojinski et al., 2014; Zhou and et al., 2026) defined by the Global Climate Observing System (World Meteorological Organization (WMO) et al., 2022). Prominent examples are the European Space Agency's (ESA's) Soil Moisture and Ocean Salinity (SMOS) mission (Kerr et al., 2010) launched in 2009, and the National Aeronautics and Space Administration's (NASA's) Soil Moisture Active Passive (SMAP) (Entekhabi et al., 2010) missions launched in 2015. Both missions are operational to date, providing unique and indispensable information on the state of the Earth's surface layer; especially on soil moisture and freeze/thaw state, forest biomass, and sea salinity and sea ice thickness.

As other microwave missions, SMOS and SMAP provide global, weather independent, and high temporal resolution with global revisit time between ~ 3 days at the equator and daily to sub-daily on high latitudes. However, in contrast to other

https://doi.org/10.5194/egusphere-2026-2927
Preprint. Discussion started: 31 July 2026

microwave frequencies, L-band BTs are highly sensitive to the volumetric content of liquid water in the Earth's surface layer and are less affected by scattering than active (radar) measurements at the same frequency. However, one of the main challenges of passive L-band observations arises from their coarse spatial resolution, a fundamental hindrance resulting from the practical limitation of deploying large antenna reflectors in space (Ulaby et al., 1981).

A variety of conceptually different retrieval approaches are used in the passive microwave remote sensing. Empirical methods use statistical relationships between observations and geophysical variables of interest (e.g., (Njoku and Entekhabi, 1996)), while change detection approaches and threshold detection algorithms exploit temporal differences to identify anomalies or geophysical state changes (e.g., (Piles et al., 2009; Rautiainen et al., 2016)). Machine learning techniques are employed to infer geophysical parameters directly from the complex, nonlinear patterns present in the observed BTs (e.g., (Rodriguez-Fernandez et al., 2015; Kumawat et al., 2025b, a)). Inversion-based retrieval approaches rely on the numerical inversion of physics-based forward models to identify the set of geophysical parameters that best reproduces the observed BTs through simulated BTs (e.g., (Kerr et al., 2012; Holmberg et al., 2024; Ortet et al., 2025)), and data assimilation methods (e.g., (Lannoy and Reichle, 2016; Reichle et al., 2017; Rodríguez-Fernández et al., 2019)) combine this with physical process models to improve retrievals. Although the microwave emission model (MEM) acts as the forward operator in inversion-based retrievals and data assimilation, they can also support any other type of retrieval approach by enabling performance evaluation or generating training datasets.

For the large footprints typically observed by space-borne L-band radiometers, modeling BT over land surfaces is challenging over heterogeneous natural landscapes. The use of a forward operator in inversion-based passive microwave retrievals imposes two limitations: first, a computational threshold, particularly in operational applications due to large data volumes; second, a structural complexity threshold arising from limited information content to constrain complex parameterizations. Accordingly, the forward operators used to simulate footprint-scale BTs provide only a crude approximation of the true scene-integrated radiative behavior. In practice, current MEMs used in inversion-based passive microwave retrievals rely on substantial simplifications of the observed scene and its radiative behavior, introducing modeling errors. These modeling errors propagate into errors and uncertainties in the retrieved geophysical variables. Therefore, improving existing MEMs and developing new ones for forward modeling of BTs is essential for advancing the field, particularly through enhanced physical realism and improved predictive capability.

Since the launch of the SMOS satellite, one of the most widely-used L-band forward operator was based on the so-called $\tau-\omega$ radiative transfer (Mo et al., 1982). It represents a zeroth-order approximation of the radiative transfer equation and it is limited to the situation of a single vegetation layer above an infinite half-space representing the ground. An inherent assumption of the $\tau-\omega$ model is that the reflectivity of the upper interface of the vegetation can be neglected. This so-called "soft-layer" assumption is justified at the L-band for virtually all vegetation types, even for very dense forests. Furthermore, multiple reflections between the vegetation layer and the ground interface are omitted, and effects associated with volume scattering within vegetation is simplified. The $\tau-\omega$ model expresses the upwelling BT at an nadir observation angle θ and at horizontal or vertical polarization $p = \mathrm{H}, \mathrm{V}$ as a function of effective physical temperatures and a set of radiative transfer

https://doi.org/10.5194/egusphere-2026-2927
Preprint. Discussion started: 31 July 2026

parameters characteristic of the observed scene:

$$T_{\mathrm{B}}^{p,\theta} = (1-\Gamma_{\mathrm{g}}^{p,\theta})t_{\mathrm{v}}^{\theta}T_{\mathrm{g}} + (1-t_{\mathrm{v}}^{\theta})(1-\tilde{\omega}_{\mathrm{v}})T_{\mathrm{v}} + \Gamma_{\mathrm{g}}^{p,\theta}t_{\mathrm{v}}^{\theta}(1-t_{\mathrm{v}}^{\theta})(1-\tilde{\omega}_{\mathrm{v}})T_{\mathrm{v}} + t_{\mathrm{v}}^{\theta}\Gamma_{\mathrm{g}}^{p,\theta}t_{\mathrm{v}}^{\theta}T_{\mathrm{sky}}. \quad (1)$$

The radiative transfer parameters of the vegetation layer (assumed to be isotropic and homogeneous) are the single scattering albedo $\tilde{\omega}$ and the vegetation optical depth $\tilde{\tau}$. The latter defines the one-way vegetation transmissivity $t_{\mathrm{v}}^{\theta} = \exp(-\tilde{\tau}_{\mathrm{v}}/\cos\theta)$. The radiative transfer parameter of the ground is expressed with its surface reflectivity $\Gamma_{\mathrm{g}}^{p,\theta}$ that can be simulated on the basis of Fresnel equations, for instance. The effective physical temperatures of the ground and the vegetation are indicated as T_{g} and T_{v}, respectively. T_{sky} is the downwelling sky radiance at L-band, which includes both the radiation emitted by the atmosphere and the cosmic background radiation attenuated by the atmosphere (Pellarin et al., 2003).

The $\tau-\omega$ model serves as the core of different forward operators implemented in operational SMOS and SMAP retrieval approaches over land: Current SMOS soil moisture algorithms (Kerr et al., 2012; Fernandez-Moran et al., 2017; Al Bitar et al., 2017) employ derivatives of the L-band Microwave Emission of the Biosphere (L-MEB) model (Wigneron et al., 2007) as forward operators, whereas SMAP soil moisture algorithms use slightly different forward operators (Entekhabi et al., 2010, 2025), which are also based on the $\tau-\omega$ model. These approaches have produced a long list of scientific achievements, yet some challenges remain, in particular related to i) forests (Colliander et al., 2026) and ii) cryosphere applications, such as soil freeze/thaw. A common challenge in cryosphere applications arises from the complex layered structures (e.g., frozen and thawed soil, snow, and frozen water bodies with ice layer and snow layers) and surface reflections, which exceed the capabilities of zeroth-order $\tau-\omega$ model.

The concept of the two-stream (2S) radiative transfer (see e.g., Chapter 10 of (Ishimaru, 1978)) has been used in a previously published microwave emission model (Wiesmann and Mätzler, 1999; Mätzler and Wiesmann, 1999, 2014) of layered snow pack with a focus on higher microwave frequencies. Based on this multi-layer 2S approach, Schwank et al. (2014) introduced L-band-specific 2S L-MEM applicable to ground covered with an arbitrary number of snow layers. Because most structures in snow are orders of magnitudes smaller than the L-band wavelength ($\lambda \sim 15\,\mathrm{cm} - 30\,\mathrm{cm}$), this 2S L-MEM neglects volume scattering. Its use was first demonstrated for snow-covered ground in a modeling study (Schwank et al., 2015) and in an empirical study based on tower-mounted L-band BT observations (Lemmetyinen et al., 2016). Schwank et al. (2018) extended the 2S L-MEM to explicitly include vegetation, thereby broadening its applicability to a wider range of land surface scenarios. The 2S L-MEM has two distinctive advantages over the contemporary $\tau-\omega$ based MEMs: i) It's modeling of scattering mechanism are more realistic, taking into account the multiple reflection and scattering within and inside the layers. ii) It has an intrinsic ability to model an arbitrary number of layers, thus representing more complex scenarios such as dense multi-layer vegetation, freezing soil, and layered snow. The computational cost of forward operators based on the 2S L-MEM is sufficiently low to allow their use in inversion-based retrievals using satellite data at a global scale. Accordingly, the 2S L-MEM has been applied in multiple studies, both using tower-based close-range BTs (Lemmetyinen et al., 2016; Naderpour et al., 2017, 2021; Wu, 2022) and in applications to satellite-based BTs (Li et al., 2020; Houtz et al., 2021; Holmberg et al., 2024; Schwank et al., 2024; Ortet et al., 2025; Holmberg et al., 2025).

https://doi.org/10.5194/egusphere-2026-2927
Preprint. Discussion started: 31 July 2026

While the 2S L-MEM was established in the mid-2010s and has been applied in multiple case studies, a comprehensive reference paper describing the model, particularly in the context of modeling satellite-observed L-band BTs, is lacking. This manuscript therefore aims to provide a consolidated and structured description of the 2S L-MEM, its components, and its application to modeling satellite-observed BTs. Specifically, the paper aims to i) review the previously published yet underused 2S L-MEM in L-band radiometry, ii) demonstrate its use in the context of passive L-band satellite observations, and iii) evaluate its agreement with satellite BT measurements from the SMOS and SMAP missions through selected use cases. Furthermore, we discuss key modeling aspects and the associated uncertainties within the context of these case studies.

2 Microwave Emission from Layered Systems

In passive microwave remote sensing, the radiation measured by an radiometer is expressed as an antenna temperature T_A. Conceptually, the antenna temperature observed in direction u is modeled as the convolution of the antenna gain pattern, $\mathcal{G}(\cdot)$, with the brightness temperature (BT) field $T_\mathrm{B}(u') = T_\mathrm{B}(r_\mathrm{obs}, u')$ at the point of observation

$$T_\mathrm{A}(u) = \int_{\mathbb{S}^2} T_\mathrm{B}(u')\mathcal{G}(u'-u)\mathrm{d}s(u'), \tag{2}$$

The BT field $T_\mathrm{B}(r,u)$ represents the propagating radiation, and is a function of the spatial coordinate $r \in \mathbb{R}^3$ and the propagation direction unit vector $u \in \mathbb{S}^2$.

Within the context of modeling satellite observed BT data, it is reasonable to assume a narrow gain pattern $\mathcal{G}(\cdot)$. Although the gain pattern beam must be narrow, due to the large distance between the satellite and the observed surface, the surface area from which the radiation emits is large (typically $40-100$ km diameter in the context of L-band satellite observations). Therefore, the observed scene over land surfaces is often heterogeneous in terms of land cover types and geophysical properties.

By approximating $u' \approx u$ and assuming azimuthal symmetry, the observed temperature T_A in Eq. (2) can be expressed as an integral over the BT field $T_\mathrm{B}^\theta(r)$ on the Earth's surface

$$T_\mathrm{A}^\theta = \int_{\mathrm{area}} T_\mathrm{B}^\theta(r)G(r)\mathrm{d}r, \tag{3}$$

where $G(r)$ is the measurement gain pattern on the observed part of the Earth's surface and θ is the zenith angle of u. While Eq. (3) represents the forward operator for the satellite observation T_A^θ, the integrand $T_\mathrm{B}^\theta(r)$ represents the local (point wise) observation operator. The coordinate dependence of $T_\mathrm{B}^\theta(r)$ comes from the spatial variability of the land cover type (determining which kind of model configuration is used to simulate T_B^θ) and geophysical properties (determining the values of the inputs to the model used to simulate T_B^θ).

This section gives a review of the previously established methods and framework to model the local forward operator $T_\mathrm{B}^\theta(r)$; the multi-layer setup, its parameterization in terms of its dielectric-, scattering-, and temperature properties, and modeling of the upwelling BT from this layered system using the L-band-specific two-stream microwave emission model (2S L-MEM). Later, in Section 3.1, the link between the dielectric- and geophysical variables are outlined.

https://doi.org/10.5194/egusphere-2026-2927
Preprint. Discussion started: 31 July 2026

The upwelling BT from a sufficiently small homogeneous area is modeled by considering a system of homogeneous layers, each representing a specific geophysical medium, such as soil, snow, or vegetation. The stack of finite, yet arbitrary number of layers, is limited by the half-infinite layer below the system (substrate) and the half-infinite layer above the system (superstrate). Each layer, including the substrate and the superstrate, emit radiation according to their respective radiative transfer properties and physical temperatures. The emitted radiation propagates through the layered medium, and is affected by interface reflections, volume scattering, and absorption. The result of a MEM is the upwelling radiation in a zenith angle, computed from the geophysical properties of the layers. This task has three parts:

1) To convert the geophysical variables of each layer into their effective dielectric constant and, optionally, scattering properties

2) To convert the layers dielectric properties into associated radiative transfer parameters.

3) From the radiative transfer parameters, to solve the radiative transfer problem for the upwards propagating radiation at a given propagation angle and polarization.

Similar to the conceptual structure used in Picard et al. (2018), these three steps are here referred to as the dielectric, electromagnetic, and radiative transfer models, respectively.

This section focuses on the electromagnetic and radiative transfer sub-models, while the dielectric sub-models are over viewed in section 3.1. It should be noted that this sort of end-to-end paradigm of modeling the observation from the final variables of interest is not the only possible approach. Some remote sensing problems are solved by first retrieving an intermediate electromagnetic, radiative transfer, or heuristic model parameter, which are then translated into the geophysical variables of interest using different regression approaches (e.g., (Rodriguez-Fernandez et al., 2018; Vittucci et al., 2019)).

2.1 Single Layer

The model that governs the BT field inside a single layer is the radiative transfer equation (see e.g, (Tsang et al., 2000)). Assuming azimuthal symmetry, the BT field $T_\mathrm{B}(z,\mu)$ can be expressed as a function of the depth z and the cosine of the propagation direction zenith angle $\mu = \cos\theta$. Fixing $\mu > 0$ and defining upwards $T_\mathrm{B}^{\uparrow}(z,\mu) = T_\mathrm{B}(z,\mu)$ and downwards $T_\mathrm{B}^{\downarrow}(z,\mu) = T_\mathrm{B}(z,-\mu)$ propagating components, the radiative transfer equation can be written as

$$\mu\frac{\partial T_\mathrm{B}^{\uparrow}}{\partial z} = -\kappa_\mathrm{e}T_\mathrm{B}^{\uparrow} + \kappa_\mathrm{a}T + \kappa_\mathrm{s}I^{\uparrow}, \tag{4a}$$

$$-\mu\frac{\partial T_\mathrm{B}^{\downarrow}}{\partial z} = -\kappa_\mathrm{e}T_\mathrm{B}^{\downarrow} + \kappa_\mathrm{a}T + \kappa_\mathrm{s}I^{\downarrow}. \tag{4b}$$

Variables κ_a and κ_s are the absorption and scattering coefficients, respectively, defining the extinction coefficient as $\kappa_\mathrm{e} = \kappa_\mathrm{a} + \kappa_\mathrm{s}$. The layer's physical temperature is denoted as T. The upwards scattering $I^{\uparrow}$ and downwards scattering $I^{\downarrow}$ integrals

https://doi.org/10.5194/egusphere-2026-2927
Preprint. Discussion started: 31 July 2026

are given by

$$I^{\uparrow} = \int_0^1 \Phi_{\mathrm{F}}(\mu;\mu') T_{\mathrm{B}}^{\uparrow}(z,\mu')\mathrm{d}\mu' + \int_0^1 \Phi_{\mathrm{B}}(\mu;\mu') T_{\mathrm{B}}^{\downarrow}(z,\mu')\mathrm{d}\mu', \tag{5a}$$

$$I^{\downarrow} = \int_0^1 \Phi_{\mathrm{F}}(\mu;\mu') T_{\mathrm{B}}^{\downarrow}(z,\mu')\mathrm{d}\mu' + \int_0^1 \Phi_{\mathrm{B}}(\mu;\mu') T_{\mathrm{B}}^{\uparrow}(z,\mu')\mathrm{d}\mu'. \tag{5b}$$

The $\Phi_{\mathrm{F}}(\mu,\mu')$ and Φ_{B} are the forward and the backwards scattering parts of the normalized two dimensional scattering phase function. The above formulation uses a symmetry of the two dimensional scattering phase function, assuming that the medium has no preferred up/down orientation for scattering.

The 2S MEM is obtained by assuming $\Phi_{\mathrm{F}}(\mu;\mu') = 0$ and $\Phi_{\mathrm{B}}(\mu;\mu') = \delta(\mu-\mu')$, where $\delta(\cdot)$ denotes the Dirac delta function. Under this assumption, the two dimensional radiative transfer Equations (4a,4b) and (5a,5b) have a closed form solution for a homogeneous layer. From this solution, the following layer equations, linking the boundary values of the upwards and downwards propagating BT fields, are obtained (see Appendix A for derivation and the original papers (Wiesmann and Mätzler, 1999; Mätzler and Wiesmann, 1999))

$$T_{\mathrm{B}}^{\uparrow}(z_1,\mu) = rT_{\mathrm{B}}^{\downarrow}(z_1,\mu) + tT_{\mathrm{B}}^{\uparrow}(z_0,\mu) + eT, \tag{6a}$$

$$T_{\mathrm{B}}^{\downarrow}(z_0,\mu) = rT_{\mathrm{B}}^{\uparrow}(z_0,\mu) + tT_{\mathrm{B}}^{\downarrow}(z_1,\mu) + eT. \tag{6b}$$

Here z_0 and z_1 are the vertical coordinates of the bottom and top interfaces of the layer. The radiative transfer properties of the layer are its internal reflectivity r, and transmissivity t, which define the layer's emissivity e, assuming thermal equilibrium. The radiative parameters r, t, and e are computed as

$$r = \frac{1-t_0^2}{1-r_\infty^2 t_0^2} r_\infty, \quad t = \frac{1-r_\infty^2}{1-r_\infty^2 t_0^2} t_0, \quad e = 1-r-t \tag{7}$$

where

$$t_0 = \exp\left(-\frac{\tau\sqrt{1-\omega^2}}{\mu}\right), \quad r_\infty = \frac{\omega}{1+\sqrt{1-\omega^2}} \tag{8}$$

and

$$\tau = d\kappa_{\mathrm{e}}, \quad \omega = \frac{\kappa_{\mathrm{s}}}{\kappa_{\mathrm{e}}}, \quad \kappa_{\mathrm{e}} = \kappa_{\mathrm{a}} + \kappa_{\mathrm{s}}. \tag{9}$$

The coefficients t_0 and r_∞ are known as the one-way layer transmissivity and the infinite thickness reflectivity, and τ and ω are the optical depth and scattering albedo.

BT fields in adjacent layers are coupled through the corresponding interface equations:

$$T_{\mathrm{B}}^{\downarrow}(z_1,\mu) = s_0 T_{\mathrm{B}}^{\uparrow}(z_1,\mu) + (1-s_0)T_{\mathrm{B}}^{\downarrow}(z_1^{+},\mu), \tag{10a}$$

$$T_{\mathrm{B}}^{\uparrow}(z_0,\mu) = s_1 T_{\mathrm{B}}^{\downarrow}(z_0,\mu) + (1-s_1)T_{\mathrm{B}}^{\uparrow}(z_0^{-},\mu). \tag{10b}$$

https://doi.org/10.5194/egusphere-2026-2927
Preprint. Discussion started: 31 July 2026

Here $T_\mathrm{B}^{\downarrow}(z_1^+,\mu)$ denotes the downwelling radiation from the layer above and $T_\mathrm{B}^{\uparrow}(z_0^-,\mu)$ denotes the upwelling radiation from the layer below. The interface reflectivities at the layer's bottom and top interfaces are denoted by s_0 and s_1, respectively.

To summarize, under the two-stream assumption, the BT streams $T_\mathrm{B}^{\uparrow,\downarrow}(z,\mu)$ are independent of each other for different values of μ. Furthermore, for a fixed propagation direction μ, the field inside a homogeneous layer can be represented by the four BT values; upwelling and downwelling BTs at the top and bottom interface (Equations (6a,6b)).

The assumption that scattering phase functions can be restricted to these discrete streams is a mathematical simplification. The physical interpretation is that, at L-band frequencies, the radiation field is partitioned into strictly upper and lower hemispheres, effectively ignoring lateral radiative fluxes. See (Wiesmann and Mätzler, 1999; Mätzler and Wiesmann, 1999) for physical interpretation that includes scattering in and from the horizontal radiation fluxes. While the two-stream assumption simplifies the calculus, it does not account for inter-angular coupling in the volume scattering. Furthermore, the two-stream approach treats the interface reflections as specular or quasi-specular. Also here, the limitation is the inability to account for inter-angular coupling; the model assumes that radiation incident at direction μ reflects only into direction $-\mu$, whereas real-world surface scattering can be diffuse due to roughness, meaning that reflected radiative energy can be redistributed across a wide angular range. Finally, the horizontal and vertical polarizations are modeled independently, neglecting the interchange of radiative fluxes at different polarizations.

2.2 Multiple Layers

Consider a system of N homogeneous layers bounded by a half-infinite substrate and a superstrate. Each of the $n = 1,\ldots,N$ layers is parameterized by the respective absorption- and scattering coefficients $\kappa_{\mathrm{a},n}$, $\kappa_{\mathrm{s},n}$, the layer thickness d_n, and the physical temperature T_n. In addition, assume that the interface reflectivities s_n (s_n is for the top interface of layer n and s_0 is for the bottom interface of the stack, i.e. the reflectivity of the substrate interface), and that the two boundary conditions; the upwelling BT below the system $T_\mathrm{B}^{\uparrow}(z_0^-,\mu)$ and the downwelling BT above the system $T_\mathrm{B}^{\downarrow}(z_N^+,\mu)$ are given. Combining the layer Equations (6a,6b) and the interface Equations (10a,10b) for each layer n forms a linear system of $4N$ equations with $4N$ unknowns (i.e., 4 streams inside each layer), which has a unique solution. An important computational remark is that the system can be reduced to a system of $2N$ equations and unknowns before numerical solution (see (Wiesmann and Mätzler, 1999) for details). The solution of the linear system provides the upwelling and downwelling radiative streams inside each N layers. In our application the value of interest is the upwelling BT above the stack of layers. This corresponds to the BT stream $T_\mathrm{B}^{\uparrow}(z_N^+,\mu)$ above the superstrate interface, i.e. at the top interface of the top most layer $n = N$. This BT is given by the associated component of the solution vector and provides the final result of the 2S MEM.

2.3 Layer parameterization

The typical characteristic dimensions of the constituents included in a layer representing soil, snow, or ice are small compared to the long L-band wavelength $15\,\mathrm{cm} \leq \lambda \leq 30\,\mathrm{cm}$. Therefore, the layer's effective complex dielectric constant ε_n can be computed using an appropriate dielectric mixing model (see e.g., (Sihvola and Kong, 2002)) and used to parameterize the layer, which is practical because:

https://doi.org/10.5194/egusphere-2026-2927
Preprint. Discussion started: 31 July 2026

1) It describes both the absorption coefficient $\kappa_{\mathrm{s},n}$ and the interface reflection s_n between adjacent layers n and $n+1$, reducing the degrees of freedom in the model's inputs.

2) Existing dielectric models express ε_n as a function of geophysical variables, thus linking them to the observed BTs.

The absorption coefficient $\kappa_{\mathrm{a},n}$ is expressed by the effective permittivity ε_n of a layer n as

$$\kappa_{\mathrm{a},n} = 2k_0 \,\mathrm{imag}\left(\sqrt{\varepsilon_n}\right), \tag{11}$$

where $k_0 = 2\pi/\lambda$ is the free-space wavenumber. The propagation angle θ_n of the radiation inside each layer n is modeled according to the Snell's law, and the specular interface reflectivities $\tilde{s}_{\mathrm{H},n}$ and $\tilde{s}_{\mathrm{V},n}$ between two adjacent layers are computed according to Fresnel's law. The specular Fresnel's reflectivities $\tilde{s}_{\mathrm{H}}$ and $\tilde{s}_{\mathrm{V}}$ are corrected empirically (Choudhury et al., 1979; Wang and Choudhury, 1981; Wigneron et al., 2007) to obtain roughness corrected reflectivities s_{H} and s_{V}, as is used in the radiative transfer model

$$\begin{aligned} s_{\mathrm{H}} &= P\exp(-h\cos^{N_{\mathrm{H}}}\theta)\tilde{s}_{\mathrm{H}} + Q\exp(-h\cos^{N_{\mathrm{V}}}\theta)\tilde{s}_{\mathrm{V}} \\ s_{\mathrm{V}} &= Q\exp(-h\cos^{N_{\mathrm{H}}}\theta)\tilde{s}_{\mathrm{H}} + P\exp(-h\cos^{N_{\mathrm{V}}}\theta)\tilde{s}_{\mathrm{V}} \end{aligned} \tag{12}$$

In the above equation $P = 1-Q$, and the parameters $h, Q, N_{\mathrm{H}}, N_{\mathrm{V}}$ characterize the interface roughness effects.

In addition, the above mentioned strong contrast between the long wavelength at L-band and the characteristic dimensions of the layer's constituents in soil, snow, and ice imply negligible scattering, such that the assumption $\kappa_{\mathrm{s}} = 0$ is justified. In particular, this simplification is not only well justified but also of considerable practical relevance. This is because modeling scattering would require detailed structural information, which is often difficult to obtain and parameterize reliably. However, for vegetation with components whose dimensions are comparable to the observation wavelength $\lambda \sim 15\,\mathrm{cm} - 30\,\mathrm{cm}$ (e.g., tree branches with diameters on the order of L-band wavelengths), volume scattering is neither negligible nor straightforward to model. Models explaining the scattering behavior (either the scattering coefficient κ_{s} or albedo ω) as a function of the dielectric and structural properties and with sufficiently low degree of complexity to be directly applicable to practical remote sensing problems do not exist at the moment. Consequently, the scattering coefficient κ_{s} or albedo ω are left as input parameters to the model, and often the volume scattering in vegetation is accounted for by empirically assigning them.

In contrast to other nominal layers such as soil, snow, or ice, vegetation layers are modeled using the soft layer assumption (Schwank et al., 2018, 2021). This includes omitting refractions and interface reflections between the layers (i.e. setting $s_{\mathrm{H}} = s_{\mathrm{V}} = 0$.) Instead of effective permittivity, and interface roughness parameters, the vegetation layers are parameterized with their optical depth $\tau = d\kappa_{\mathrm{e}}$ and single scattering albedo $\omega = \kappa_{\mathrm{s}}/\kappa_{\mathrm{e}}$, or alternatively with the column scattering $\tau_{\mathrm{s}} = d\kappa_{\mathrm{s}}$ and column attenuation $\tau_{\mathrm{a}} = d\kappa_{\mathrm{a}}$. More complex models for the radiative transfer parameters of the vegetation from basic structural and dielectric properties exist, although not directly applicable to practical remote sensing problems. One example is the Microwave Emission Model of Layered Vegetation (MEMLV, (Zhou et al., 2024)), which represents the vegetation structure statistically and treats radiative transfer as interactions with discrete dielectric cylinders representing canopy constituents (trunks, branches, and needles).

https://doi.org/10.5194/egusphere-2026-2927
Preprint. Discussion started: 31 July 2026

To summarize, the nominal layers such as soil, snow, and ice are parameterized with their layer inputs $\mathbf{v}_n = (d_n, \varepsilon_n, \kappa_\mathrm{s}/\omega_n)$ and interface inputs $\mathbf{i}_n = (h_n, Q_n, N_{\mathrm{H},n}, N_{\mathrm{V},n})$. The soft layers such as vegetation are parameterized with their volume inputs $\mathbf{v}'_n = (\tau_n, \omega_n)$ or $\mathbf{v}'_n = (d\kappa_{\mathrm{s},n}, d\kappa_{\mathrm{a},n})$. These inputs are used to compute the radiative transfer parameters of each layer, which in turn, together with the physical temperatures of each layer, are used to solve the upwelling BT from the layered system. Figure 1 shows a schematic of the described process and the layer inputs. To connect the resulting upwelling BT with the the actual geophysical variables of interest, dielectric models describing the effective complex permittivities ε_n as functions of the geophysical variables of each layers medium must be considered. Section 3 describes the specific modeling choices and the used dielectric models.

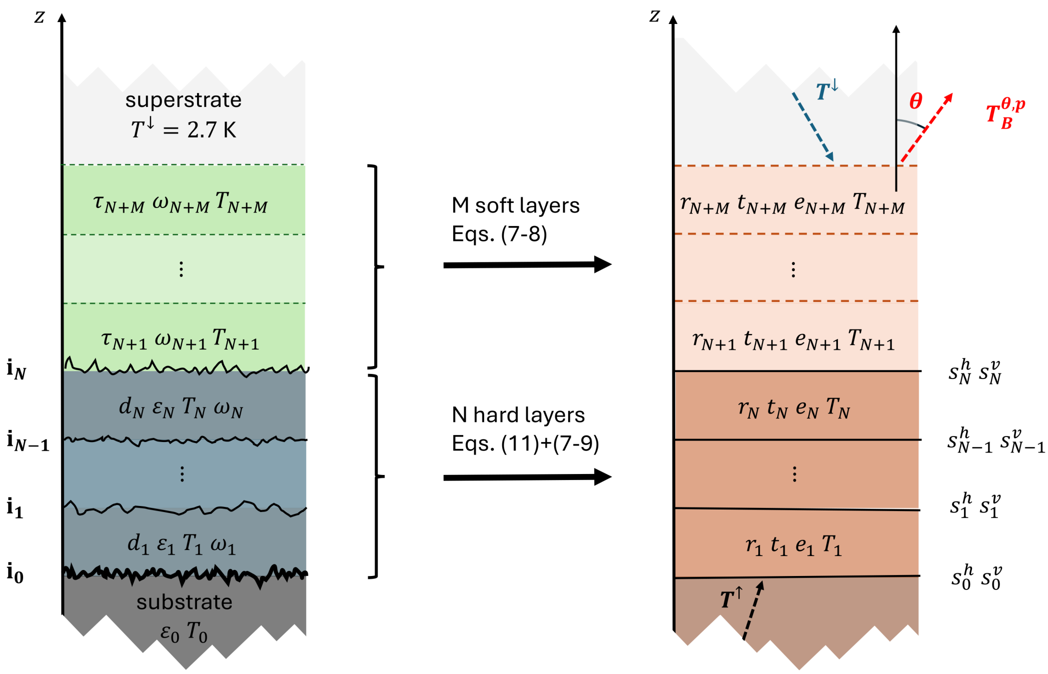

Figure 1. Schematic of the generic layered system and its inputs (left) and the corresponding 2S radiative transfer setup used to solve the upwelling BT in an observation angle θ above the system (right). Figure depicts a scenario where N hard layers (representing ground, water, ice, snow) are covered by M soft layers (representing vegetation and atmosphere). The superstrate is the cold space above the atmosphere.

245 ## 3 Land emission scenario models

The framework described in Section 2 is used to construct layered systems representing abstractions of a selection of typical natural land scenarios. An example of such a scenario would be a forested and snow covered scene, modeled by a stack of three finite layers: snow, forest, and atmosphere, together with soil substrate and cold space superstrate (see Figure 1).

https://doi.org/10.5194/egusphere-2026-2927
Preprint. Discussion started: 31 July 2026

Layer	Parameterization	Geophysical Variables	Comments
Atmosphere	$\tau_{\mathrm{atm}}, T_{\mathrm{atm}}$		Scattering omitted. Effective parameters are computed via empirical regression formulas
Vegetation	$\tau_{\mathrm{v}}, \omega_{\mathrm{v}}, T_{\mathrm{v}}$	Vegetation column water content, dry biomass, height	Soft layer assumption.
Snow	$d_{\mathrm{s}}, \varepsilon_{\mathrm{s}}, T_{\mathrm{s}}$	Mass density, liquid water content, depth	Volume scattering is omitted. Assuming specular top interface.
Ice	$d_{\mathrm{i}}, \varepsilon_{\mathrm{i}}, T_{\mathrm{i}}$		Common choice is $\varepsilon_{\mathrm{i}} = 3.18$, omitting the imaginary part. Assuming specular top interface.
Ground	$d_{\mathrm{g}}, \varepsilon_{\mathrm{g}}, T_{\mathrm{g}}, H_{\mathrm{g}}, Q_{\mathrm{g}}, N_{\mathrm{H,g}}, N_{\mathrm{V,g}}$	Soil moisture, freeze-thaw state	Scattering is omitted. Layer thickness d_{g} is not relevant if used as a substrate.
Water	$d_{\mathrm{w}}, \varepsilon_{\mathrm{w}}, T_{\mathrm{w}}, H_{\mathrm{w}}, Q_{\mathrm{w}}, N_{\mathrm{H,w}}, N_{\mathrm{V,w}}$		Scattering is omitted. Layer thickness d_{w} is not relevant if used as a substrate.

Table 1. Summary of layers representing different natural media, their parameterization, relevant geophysical variables for land surfaces on L-band, and key modeling choices and assumptions. Dry snow and ice have negligible absorption and scattering for typical land surface targets at the L-band. Therefore, in these two cases the layer thickness d and temperature T have negligible effect, and can be omitted. For meaning of the symbols, see text.

The common scenarios appearing in practical satellite remote sensing of land include ground, snow, vegetation, water, ice, and atmosphere layers. Section 3.1 describes input parameters and different modeling choices for each of the above-mentioned layers used in our implementation of the model. Section 3.2 describes how these layers are combined to form a scenario model, and how the scenario models are subsequently merged to simulate antenna temperatures representing the space-born microwave radiometer measurement for a given configuration and geometry.

3.1 Layers

3.1.1 Ground

The ground layer can act as a half-infinite substrate or as a finite layer. In the case where it acts as an half-infinite substrate, it is parameterized with its complex effective permittivity ε_{g}, temperature T_{g}, and the interface roughness parameters $\mathbf{i}_{\mathrm{g}} = (H_{\mathrm{g}}, Q_{\mathrm{g}}, N_{\mathrm{H,g}}, N_{\mathrm{V,g}})$. In this case, the physical temperature acts as the boundary condition (upwelling BT from the substrate) $T^{\uparrow}(z_0^-, \mu) = T_{\mathrm{g}}$, while ε_{g} and $\mathbf{i}_{\mathrm{g}}$ affect the reflectivity of the interface above the substrate as described in Section 2.

In the case when a ground layer is modeled as an finite layer (e.g., a finite layer of frozen ground above a thawed ground substrate), the layer thickness d_{g} is needed in addition to the above mentioned inputs. While it is common to omit volume

https://doi.org/10.5194/egusphere-2026-2927
Preprint. Discussion started: 31 July 2026

scattering ($\kappa_{\mathrm{s,g}} = 0$) in the soil layers, as soil structures are typically smaller than L-band observation wavelengths, it can be added if required.

The complex permittivity can be expressed as a function of the geophysical variables of the ground medium

$$\varepsilon_{\mathrm{g}} = f_{\mathrm{g}}(m_{\mathrm{g}}, T_{\mathrm{g}}; \beta_{\mathrm{g}}), \tag{13}$$

where m_{g} is the volumetric soil moisture (liquid-water content) and β_{g} includes any parameters appearing in the dielectric function (e.g., soil texture variables such as porosity, bulk density, and clay, sand, and silt fractions). Many such models exists, with varying basis in theoretical and empirical approaches (Hallikainen et al., 1985; Dobson et al., 1985; Peplinski et al., 1995; Mironov et al., 2009, 2010, 2017). Mätzler and Schwank (2006) describes five models for calculating ε_{g} of varying complexity and compares them. Two significant aspects to consider are the soil type that the model assumes (mineral or organic), and the valid temperature range of the model, and if it models soil freezing. Furthermore, the dielectric functions contain their own errors/uncertainties. The magnitude and effect of these uncertainties to the final modeled BTs is a topic for future studies.

While the use of a dielectric function is necessary to connect the observed or modeled BT with the actual geophysical variables, sometimes it might be more practical to consider the permittivity as an input to the model. For example, constant value could be applied for frozen soil, either from the literature (e.g., (Hallikainen et al., 1985, 1984)) or fitted to observations. In forward modeling applications, however, if in situ sensors provide direct measurements of permittivity, their use as model input may be preferable.

3.1.2 Water

For land applications, water layer will act as a substrate possibly covered by layers representing e.g. ice or vegetation. Similar to the ground substrate, a water substrate is parameterized with its complex permittivity ε_{w} and temperature T_{w}, and the interface roughness parameters $\mathbf{i}_{\mathrm{w}} = (H_{\mathrm{w}}, Q_{\mathrm{w}}, N_{\mathrm{H,w}}, N_{\mathrm{V,w}})$. In the case of water bodies, the most straight forward option is to consider a specular water-air interface characterized by $\mathbf{i}_{\mathrm{w}} = (0,0,0,0)$. However, this assumption might not be valid in case of a water body exhibiting a frozen surface layer. A simple practical choice for the complex permittivity of water at L-band is to use a value from the literature. Chapter 5 in (Mätzler et al., 2006) describes several commonly used models to compute ε_{w} as a function of T_{w}, f, and salinity S.

3.1.3 Snow and ice

A snow layer is parameterized by its thickness d_{s}, complex permittivity ε_{s} and temperature T_{s}. The geophysical variables that describe the effective permittivity of snow are the volumetric liquid water content m_{s}, mass density ρ_{s}, and T_{s}. A dielectric function expresses ε_{s} as function of the influential geophysical variables of the snow medium (see e.g., (Mätzler and Wiesmann, 2014))

$$\varepsilon_{\mathrm{s}} = f_{\mathrm{s}}(m_{\mathrm{s}}, \rho_{\mathrm{s}}, T_{\mathrm{s}}). \tag{14}$$

https://doi.org/10.5194/egusphere-2026-2927
Preprint. Discussion started: 31 July 2026

If the snow layer is considered as dry ($m_\mathrm{s} = 0\ \mathrm{m}^3/\mathrm{m}^3$), a simple regression formula for its permittivity as a function of ρ_s exists (Mätzler, 1996). As dry snow does almost not attenuate nor scatter at L-band (therefore, emission depths in dry snow can reach several hundred meters, as shown in Fig. 2 of (Mätzler, 2001)), and we do not consider coherent interference effects, d_s and T_s have no effect on its radiative transfer. Nevertheless, the presence of even a completely dry snow layer above the ground affects L-band BTs via interface reflection and refraction, as has been demonstrated theoretically (Schwank et al., 2014, 2015) and experimentally in (Lemmetyinen et al., 2016).

A key finding regarding the propagation of L-band radiation in snow is that volume scattering generally plays a minor role (Schwank et al., 2014), except in the presence of prominent macro structures (such as ice lenses) with dimensions of the order of the observation wavelength. Accordingly, assuming a scattering coefficient of $\kappa_\mathrm{s,s} = 0\ \mathrm{m}^{-1}$ for a snow layer is reasonable in most cases. This implies that at L-band the snow grain size, a relevant geophysical variable at higher frequencies, is assumed not to affect snow radiative transfer at L-band. Furthermore, in most practical circumstances it is reasonable to assume snow layer interfaces as specular; $\mathbf{i}_\mathrm{s} = (0,0,0,0)$.

Similarly for ice, a dielectric model can be considered (see e.g., Chapter 5 of (Mätzler et al., 2006)). However, a constant value from literature $\varepsilon_\mathrm{i} = 3.18$ is a practical choice in many land applications. Such choice means lossless medium, and thus the ice layer's thickness d_i and temperature T_i do not have an effect. This is not the case when the imaginary part of ice permittivity is non-zero. Again, the interface roughness in the ice-air or ice-snow interface layer can be neglected in most practical cases; $\mathbf{i}_\mathrm{s} = (0,0,0,0)$.

Hossan et al. (2025) evaluated differences in simulated BTs arising from the use of various dielectric models for wet snow permittivity. The study demonstrated that the choice of a dielectric function can lead to substantial differences in modeled L-band BTs. This underscores the uncertainty associated with the snow dielectric function, particularly in the case of wet snow.

3.1.4 Vegetation and forest

Different choices are possible to parameterize the vegetation layer. A typical choice is to use the vegetation optical depth (VOD) $\tau_\mathrm{v} = d_\mathrm{v}\kappa_\mathrm{e,v}$ and the single scattering albedo $\omega_\mathrm{v} = \kappa_\mathrm{s,v}/\kappa_\mathrm{e,v}$, where $\kappa_\mathrm{e,v} = \kappa_\mathrm{a,v} + \kappa_\mathrm{s,v}$. An alternative parameterizations is to use the column absorption and scattering coefficients $\tau_\mathrm{a} = d_\mathrm{v}\kappa_\mathrm{a,v}$ and $\tau_\mathrm{s} = d_\mathrm{v}\kappa_\mathrm{s,v}$, or the layer transmissivity t_v and reflectivity r_v (see Equations (7-9)).

At L-band, the soft-layer assumption is justified even for dense vegetation such as forests (Schwank et al., 2021), as the effective permittivity of the layer is close to unity. Consequently, interfaces to air ($\varepsilon_\mathrm{air} = 1$) or to another vegetation layer are assumed not to induce refraction; i.e., the propagation angle remains unchanged, consistent with setting $\mathrm{Re}\left(\sqrt{\varepsilon_\mathrm{v}}\right) = 1$ in the Snell's law. Moreover, reflections at a soft-layer interface are neglected, such that the interface reflectivities are assumed $s_\mathrm{H} = s_\mathrm{V} = 0$. Accordingly, the parameterization of the interface roughness of a soft layer is of no relevance.

Typically, VOD has been considered as the parameter of interest in the retrieval of vegetation parameters derived from passive microwave radiometry (Mo et al., 1982; Kerr and Njoku, 1990; Zotta et al., 2024; Mialon et al., 2020; Fan et al., 2019), while the scattering albedo has been considered an a priori fixed nuisance/calibration parameter. However, recent retrieval-

https://doi.org/10.5194/egusphere-2026-2927
Preprint. Discussion started: 31 July 2026

(Schwank et al., 2021, 2024) and modeling studies (Zhou et al., 2024) have investigated links between the effective radiative transfer parameters τ_{v} and ω_{v} with geophysical variables of the forest: Schwank et al. (2021, 2024) introduced a model for the optical depth of the type

$$\tau_{\mathrm{v}} = f_{\mathrm{v}}(m_{\mathrm{v}}, M_{\mathrm{v}}, T_{\mathrm{v}}; \beta_{\mathrm{v}}), \tag{15}$$

where m_{v} and M_{v} stand for the canopy column water content and above ground dry biomass, respectively. While this VOD-model focused on the temperature dependence of VOD, in principle it provides a function — conceptually similar to the dielectric functions for soil and snow — linking the optical depth with the geophysical variables of interest at L-band, similarly to the dielectric functions for soil expressing ground permittivity ε_{g} with soil water content.

Currently, there is no model that describes the scattering properties of a forest layer (i.e., $\kappa_{\mathrm{s},v}$ or ω_v) with a level of simplicity low enough to be directly applicable to practical retrieval problems. However, more complex electromagnetic models accounting for sophisticated forest architectures have been developed to simulate the effective radiative transfer properties, which can then be used to support and guide the retrieval process (Zhou et al., 2024; Chen and Tan, 2024).

For example, Zhou et al. (2024) developed a hybrid model (the Microwave Emission Model for Layered Vegetation; MEMLV), which is based on a combination of a tree structure model (TSM), the 2S MEM, and a discrete scatter model (DSM). MEMLV discretizes the vegetation structure into multiple vegetation layers $n = 1, \ldots, N$ based on the macro-parameters describing the crown shape, the canopy-height, and the canopy gap fraction. The TSM and the DSM are used to compute the single scattering albedo ω_n and VOD τ_n of each layer, in which the number density, dimensions and size-distribution of vegetation constituents are considered. Similar to the approach described in Section 2, the 2S MEM is used to calculate the upwelling BTs above the vegetation. Finally, an optimization procedure is used to obtain the effective radiative transfer parameters τ_{eff} and ω_{eff}, of the stack of vegetation layers representing the canopy. Although MEMLV's parameterization is too complex for direct use in practical retrievals, statistical relationships could be established between its simulated effective radiative transfer parameters $(\tau_{\mathrm{eff}}, \omega_{\mathrm{eff}})$ and bulk forest properties, namely canopy column water content m_{v} and above-ground dry biomass M_{v}. Early in the SMOS mission, equivalent propagation properties of different vegetation types (intended for use with the zeroth-order $\tau - \omega$ MEM) were estimated from BTs simulated using the matrix doubling algorithm (Ferrazzoli et al., 2003). However, approaches leveraging the 2S MEM, which allows vegetation to be represented by multiple layers, have not yet been explored. Studies based on MEMLV, therefore, represent a promising avenue for future research.

3.1.5 Atmosphere

As illustrated in Figure 1, the atmosphere is considered as the topmost layer in every scenario model. The radiative transfer in the atmosphere is represented by its optical depth τ_{atm} and its effective temperature T_{atm}. Volume scattering in the atmosphere can be omitted $\omega_{\mathrm{atm}} = 0$. Optical depth and effective temperature of the atmosphere layer are estimated using 2 meters above ground air temperature T_{air} (in units of K), humidity ϱ_{atm} (in units of g/kg), and the altitude of the footprint area above the sea level h_{asl} (in units of km) with the following empirical regression formulas originally developed by Pellarin et al. (2003)

https://doi.org/10.5194/egusphere-2026-2927
Preprint. Discussion started: 31 July 2026

Coef.	Value	Unit	Coef.	Value	Unit
a_0	5.051×10^0	–	b_0	-4.011×10^0	–
a_1	1.727×10^{-3}	K^{-1}	b_1	-3.34×10^{-3}	K^{-1}
a_2	-6.9×10^{-3}	km^{-1}	b_2	-2.193×10^{-1}	km^{-1}
a_3	1.92×10^{-3}	$\mathrm{kg\ g}^{-1}$			

Table 2. Regression coefficients for the atmospheric effective temperature and optical depth regression formulas in Eq. (16).

and used later (with different parameter values) by Schwank et al. (2015).

$$\begin{aligned} T_{\mathrm{atm}} &= \exp(a_0 + a_1 T_{\mathrm{air}} + a_2 h_{\mathrm{asl}} + a_3 \varrho_{\mathrm{atm}})\ [K] \\ \tau_{\mathrm{atm}} &= \exp(b_0 + b_1 T_{\mathrm{air}} + b_2 h_{\mathrm{asl}})\ [-]. \end{aligned} \tag{16}$$

The used coefficients from (Schwank et al., 2015) are reported in Table 2. The superstrate above the atmosphere is the cold space. The known cosmic background radiation (Wilson, 1979) acts as the downwelling boundary condition $T_{\downarrow} = 2.7$ K. With the atmosphere as the topmost layer, upwelling BT at the top of the atmosphere (i.e., at the satellite radiometer antenna) is simulated following the approaches outlined in Section 2.

3.2 Modeling the satellite-observed antenna temperature

In what follows we use γ to denote observation configuration of a particular satellite measurement, including (but not necessarily limited to) the observation angle θ, polarization p, and the antenna footprint pattern. As the antenna temperature T_{A}^{γ} measured by a space-borne radiometer is a convolution integral of BTs $T_{\mathrm{B}}^{\gamma}(\cdot)$ over a large footprint and the antenna's gain pattern $G(\cdot)$ (Eq. 3), it may include contributions from various different land cover types and surface conditions, each of which are represented by an appropriate scenario model. To list common scenario models over land, we first distinguish between different substrates: in all common cases it is either water or ground. A ground substrate can be covered by snow and/or vegetation, while a water substrate can be covered by ice or ice and snow layers. Such layer configurations define the common scenario models, which can be made more complex by increasing the number of layers of any medium. Important use cases for multiple layers of the same natural medium include freezing soil (e.g., thawed soil substrate below a frozen soil layer), melting snow (e.g., snow wetness appearing in different parts of the snow pack), and vegetation (separate modeling of vegetation understory and forest, or modeling dense forest canopies represented by multiple vegetation layers).

We defined seven common scenario models to demonstrate and to constrain the explanation of modeling the satellite-observed antenna temperature. The scenario models are referred to as by codes: G, GS, GV, GSV, W, WI, and WIS. The seven scenarios are composed of five basic layer types: (G)round, (W)ater, (S)now, (V)egetation, and (I)ce. For example GSV refers to a scenario model with ground substrate covered by snow, vegetation, and atmosphere layers. Since the atmospheric top-layer is part of all seven model scenarios and is parameterized using the same radiative transfer parameters τ_{atm} and T_{atm}, it has been omitted from the scenario names. The collection $\mathcal{C} = \{\mathrm{G}, \mathrm{GS}, \mathrm{GV}, \mathrm{GSV}, \mathrm{W}, \mathrm{WI}, \mathrm{WIS}\}$ denotes the set of scenarios

https://doi.org/10.5194/egusphere-2026-2927
Preprint. Discussion started: 31 July 2026

that are considered in this section. In this section we restrict ourselves to this set of standard scenarios to maintain a clear and focused description, but more complex multi-layered scenario models are used in later case studies.

The local observation operator, denoted as $T_{\mathrm{B}}^{\gamma}(r)$ in Eq. (3), depends on the location r through the scenario (land cover type) 385 $\mathbf{S}(r) \in \mathcal{C}$ and it's geophysical variables $\mathbf{X}(r) \in \mathbb{X}$, i.e., $T_{\mathrm{B}}^{\gamma}(r) = T_{\mathrm{B}}^{\gamma}(\mathbf{X}(r), \mathbf{S}(r))$. While the relevant inputs between different scenario models vary, we consider $\mathbf{X}(r)$ to include all relevant inputs to every scenario model considered in $\mathcal{C}$. Thus the state space $\mathbb{X} \subset \mathbb{R}^K$ for some K.

The model (not including observation errors) for the satellite-observed antenna temperature $T_{\mathrm{A}}^{\gamma}(\mathbf{X}, \mathbf{S})$ observed from the fields $\mathbf{X}$ and $\mathbf{S}$ is therefore given by

390 $$T_{\mathrm{A}}^{\gamma}(\mathbf{X}, \mathbf{S}) = \int\limits_{\text{area}} T_{\mathrm{B}}^{\gamma}(\mathbf{X}(r), \mathbf{S}(r)) G^{\gamma}(r) \mathrm{d}r, \tag{17}$$

Here $T_{\mathrm{B}}^{\gamma}(x, s)$ is the scenario model (local forward operator) corresponding to scenario $s = \mathbf{S}(r)$, input $x = \mathbf{X}(r)$. Function $G^{\gamma}(r)$ is the satellite observation footprint patterns density function on the Earth's surface.

Often in practice, Eq. (17) is further approximated depending on the application. For the evaluation of the forward model simulated BTs with in situ observations and satellite data, the idealized circumstances are that there is a large number of sites 395 distributed within the satellite footprint, and that each site $m = 1, \ldots, M$ measures input $x_m = \mathbf{X}(r_m)$ to a model scenario $s_m = \mathbf{S}(r_m)$ which represents conditions at site m. Then, the integral in Eq. (17) can be approximated with

$$T_{\mathrm{A}}^{\gamma}(x, s) \approx \sum_{m=1}^{M} w_m T_{\mathrm{B}}^{\gamma}(x_m, s_m). \tag{18}$$

The weights w_m are the representativeness of each site. In ideal circumstances, when the number M of sites is large, and the sites are distributed according to the spatial density pattern $G^{\gamma}(\cdot)$, uniform weights $w_m = 1/M$ are justified. Since this is rarely 400 the case in practice, other weighting schemes based on the locations and land cover classes of the sites are used.

On the contrary, when considering a retrieval problem, a common approximation is to omit the heterogeneity of the geophysical variables by assuming a homogeneous field ($\mathbf{X}(r) = x \in \mathbb{X}$ for every r) reducing the Eq. (17) to a sum over the scenario models (i.e., land cover types)

$$T_{\mathrm{A}}^{\gamma}(x) \approx \sum_{s \in \mathcal{C}} w^{\gamma}(s) T_{\mathrm{B}}^{\gamma}(x, s), \tag{19}$$

405 where the radiometric weights $w(s)$ for the scenarios $s \in S$ are given by

$$w^{\gamma}(s) = \int\limits_{\text{area}} 1_s(\mathbf{S}(r)) G^{\gamma}(r) \mathrm{d}r. \tag{20}$$

Here $1_s(\mathbf{S}(r))$ is the indicator function; $1_s(\mathbf{S}(r)) = 1$ for $\mathbf{S}(r) = s$ and $1_s(\mathbf{S}(r)) = 0$ otherwise. In practice these are computed based on the satellite footprint pattern $G^{\gamma}(\cdot)$ and auxiliary land cover and snow information maps used to define the spatial field $\mathbf{S}(r)$. This process is not considered a part of the model as we consider the weights $w(s)$ as inputs, but it is outlined in 410 Appendix B. The simplified version in Eq. (19) has the practical advantage of reduced complexity (number of unknowns). Yet this implicit regularization introduces modeling and retrieval errors related to the heterogeneity of the geophysical variables within the satellite footprint.

https://doi.org/10.5194/egusphere-2026-2927
Preprint. Discussion started: 31 July 2026

4 Comparison of modeled and satellite-observed BTs

To demonstrate the capability of the modeling framework presented in Sections 2 and 3, this section compares antenna temperatures simulated with the forward operator to corresponding satellite observations for three case studies at distinct sites with available in situ data. Section 4.1 shows the use case from a complex arctic Boreal forest site located in Northern Finland and using SMOS L1C BT data. Section 4.2 presents a case study focusing on an arctic site located in Alaska and applying SMOS L3 BT data, with particular emphasis on stable winter conditions and the influence of sub-snow soil temperature to the BT. Section 4.3 demonstrates the performance of modeled SMAP BTs from Massachusetts, one of the SMAP core validation sites in Northern America.

4.1 Simulation of SMOS L1C BTs over the Sodankylä site

The SMOS L1C (European Space Agency, 2009) is the primary BT data set used in the operational L2 science products of the SMOS mission (Kerr et al., 2010, 2012; Reul et al., 2020; Boutin et al., 2021). For an individual SMOS overpass and grip point location, the L1C BT data is expressed as a series of observations $T_{\mathrm{B}}(\gamma_k)$, $k = 1,\ldots,K$, where the number of observations K varies between the overpasses. The observation configuration γ_k includes information on the observation angle, polarization, rotation angle from ground to satellite reference frame, and the footprint pattern orientation and dimensions (elliptic major and minor axis), all expressed in the L1C data. The data is given in the satellite reference frame. To compare BTs simulated by the forward operator with corresponding observations at horizontal and vertical polarization, the former need to be transformed into the satellite reference frame (see e.g, (Martín-Neira et al., 2002; Kerr et al., 2011)) via

$$\begin{bmatrix} T_{\mathrm{B,X}} \\ T_{\mathrm{B,Y}} \end{bmatrix} = \begin{bmatrix} \cos^2\alpha & \sin^2\alpha \\ \sin^2\alpha & \cos^2\alpha \end{bmatrix} \begin{bmatrix} T_{\mathrm{B,H}} \\ T_{\mathrm{B,V}} \end{bmatrix} \tag{21}$$

where $\alpha = \alpha_{\mathrm{geom}} + \alpha_{\mathrm{ionos}}$ denotes the total rotation angle, composed of the geometric rotation α_{geom} and the ionosphere-induced rotation α_{ionos} of the surface radiance.

To demonstrate the performance of the 2S L-MEM forward operator in modeling satellite BTs, a one-year-long time series of SMOS L1C BTs was extracted over the Sodankylä region from October 2019 to October 2020. The corresponding BT time series was modeled using data from the in situ stations located in the Sodankylä region (Ikonen et al., 2016). For each station, in situ measurements of soil permittivity and temperature from the multiple sensors were used as inputs to the 2S L-MEM forward operator to simulate corresponding BT time series measured by a space-borne radiometer. Figure 2 shows approximately 120 km × 120 km section of the CCI land cover map of the Sodankylä region. The locations of the here used in situ stations are marked with white triangles. Ellipses indicate the 90% footprints at different observation angles from a single SMOS overpass.

A scenario model adapted to the local conditions of each station was used; scenario model GV and GSV (defined in Section 3.2) were used for the station with forest vegetation on ground during summer and winter (including a snow layer), respectively. Similarly, scenario models G and GS were used for open (non-forested) sites. The radiative transfer parameters of the vegetation layer in the forested scenario models GV and GSV were set to $\omega_{\mathrm{v}} = 0.1$ and $\tau_{\mathrm{v}} = \tau_{\mathrm{v}}(T_{\mathrm{v}};\beta)$ simulated using the L-VOD model of (Schwank et al., 2021, 2024). The parameterization β of the L-VOD model was obtained from previously

https://doi.org/10.5194/egusphere-2026-2927
Preprint. Discussion started: 31 July 2026

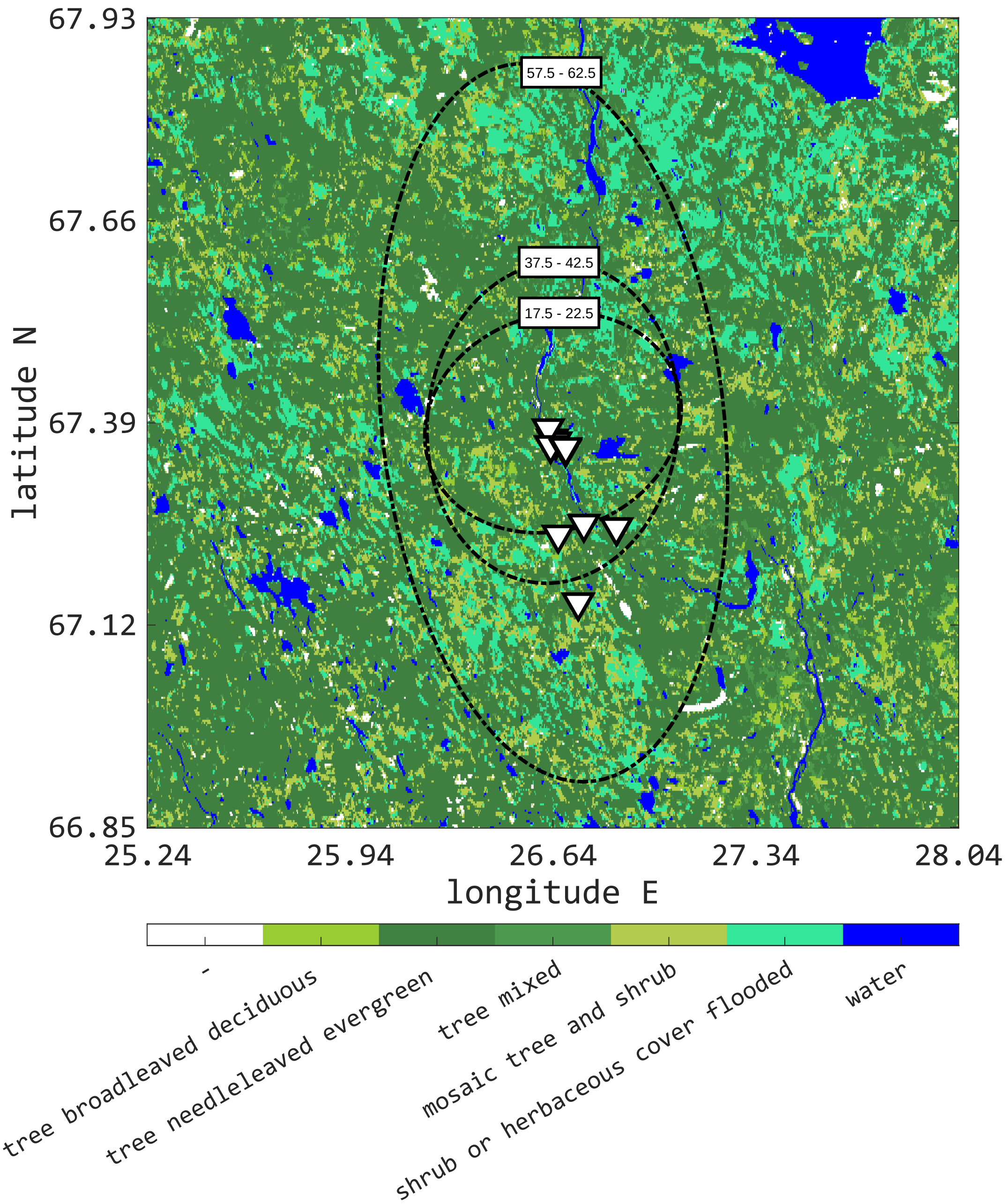

Figure 2. Approximately 120 km × 120 km area including the Sodankylä region. Background map is the CCI land cover. The white triangles show the locations of in situ soil moisture stations. Ellipses show SMOS L1C footprints for the observation angles $\theta = 20^\circ, 40^\circ, 60^\circ$ and for a single satellite overpass. The shown footprints correspond to the areas within which 90% of the signal originates from. The Tähtelä research station is located approximately at the center of the SMOS footprints.

https://doi.org/10.5194/egusphere-2026-2927
Preprint. Discussion started: 31 July 2026

performed calibration against upward-looking ground based radiometer observed VOD values in the Sodankylä region (Kontu, 2022). The resulting simulated τ_{v} provides an input for the vegetation layer parameterization, capturing the strong temperature dependence of VOD, particularly near and below the freezing point (Schwank et al., 2021, 2024). Although calibrated, the modeled τ_{v} is affected by errors from the representativeness of the local upward-looking radiometer measurements from below canopy and spatial heterogeneity (e.g., due to variable biomass within the SMOS footprints over Sodankylä). Effects of this heterogeneity on the simulated BTs for the GV and GSV scenario models are beyond the scope of this study and may be explored in future work.

In addition to the Sodankylä in situ stations, we considered a contribution from water bodies and water courses with the scenario models W and WIS during summer and winter, respectively. A temperature dependent water permittivity $\varepsilon_{\mathrm{w}} = \varepsilon_{\mathrm{w}}(T_{\mathrm{w}})$ was used to parameterize the water substrate with temperature T_{w} assumed as the layer 1 (0–7 cm) soil temperature from the ERA5 re-analysis data product, but not allowing it to drop below 275 K.

To represent the radiative transfer within the ice layer, its permittivity was assumed to be $\varepsilon_{\mathrm{i}} = 3.18$. This choice implies that the ice layer does not emit nor absorb radiation, so neither its temperature T_{i} nor its thickness d_{i} affects the simulation. In the GSV and WIS scenario models, the snow layer was assumed dry with a density of $\rho_{\mathrm{s}} = 250\ \mathrm{kg/m^3}$. As discussed in Section 3.1.3, assuming the snow layer to be completely dry is expected to introduce substantial errors in the modeled BTs when this assumption is violated, particularly during the early spring period when wet snow is likely to be present.

The modeled BTs from each station were further averaged into land cover class specific BTs, corresponding to four classes: open/forested with nominal/wetland soil. Figure 3 shows the simulated time series of land-cover-averaged BTs in the satellite reference frame (X and Y) at the observation angle $\theta = (40 \pm 2.5)^{\circ}$, compared with the corresponding SMOS L1C BT observations. Figure 3 demonstrates the distinct difference in the dynamics between nominal and wetland sites between each other, and compared to SMOS. Furthermore, the strong contrast between the wetland and nominal sites highlight the importance of modeling wetlands explicitly.

The modeled land cover averaged BTs were further averaged into a satellite scale BT by applying land cover weights estimated from the SMOS L1C footprint pattern data; static weights $w_{\mathrm{open}} = 30\%, w_{\mathrm{forest}} = 67\%$, and $w_{\mathrm{water}} = 3\%$ were used. Areal fraction of the wetlands were manually tuned into a realistic value; 50% of the open area was modeled as wetland, i.e., 15% of the total area. Figure 4 shows the comparison between the simulated averaged BT time series and the corresponding SMOS L1C observations. Figure 5 shows the scatter plot comparing the modeled and observed BTs. Whereas the time series Figures 3 and 4 are limited to instances with small rotation angle α for visual clarity, in the scatter plots in Figure 5 all data instances are shown. Table 3 shows the standard statistics associated with Figure 5.

The over all visual agreement between the modeled and observed BTs seen in Figure 4 is good; the modeled BTs follow the seasonal dynamics of the observed BTs and the absolute level match on a visual level. However, the periods expected to be influenced by wet snow (end of snow periods, shown by the horizontal black bars) demonstrate differences between the two: the modeled BT time series does not show the same drop in its values as is seen in the observed BTs. Statistics in Table 3 shows that the mean difference between the modeled and observed BTs is low ($0.2 - 3.2$ K), but the standard deviation of the difference is larger ($7.9 - 9.5$ K) than what would be expected based on the SMOS noise level alone (~ 4 K).

https://doi.org/10.5194/egusphere-2026-2927
Preprint. Discussion started: 31 July 2026

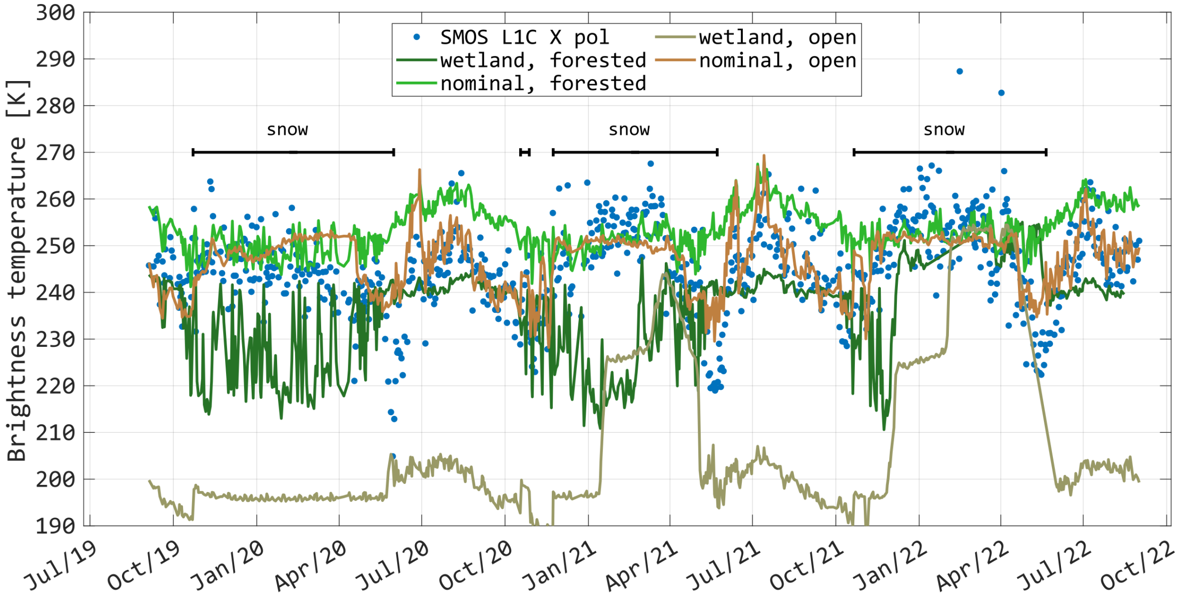

(a)

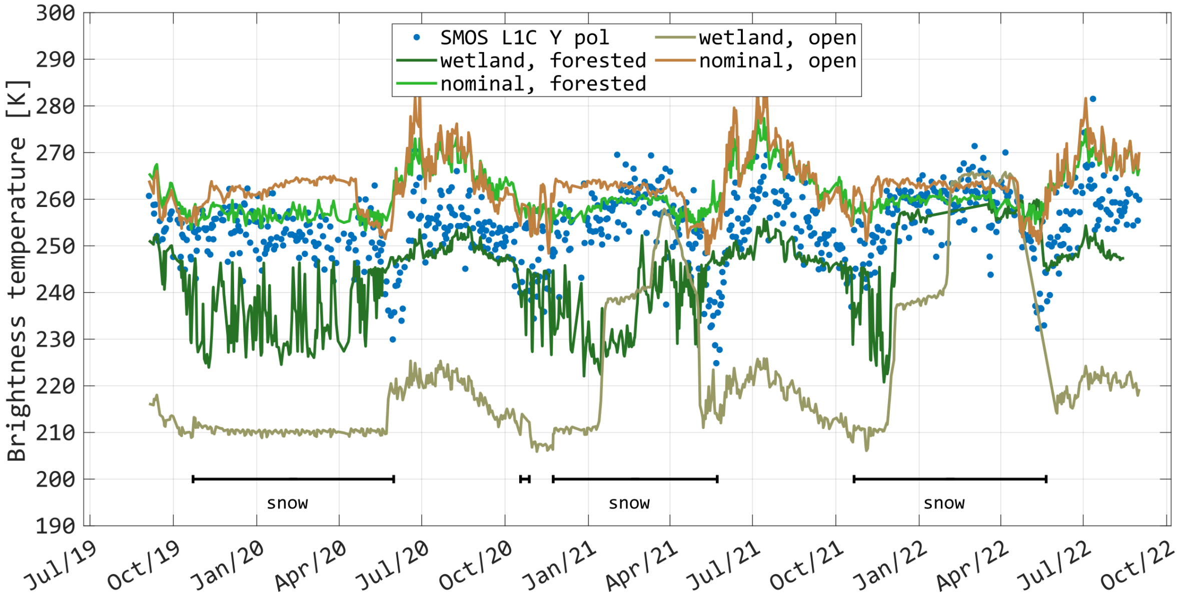

(b)

Figure 3. Time series of the SMOS L1C BTs from a grip point located in the Sodankylä region (DGG D4030676) and BTs modeled with the forward operator using in situ sensor data, and averaged into four different land cover class, (a) X polarized and (b) Y polarized BT. BTs correspond to the observation angle $\theta = (40 \pm 2.5)^{\circ}$. For visual purposes only values corresponding to total rotation angle α with $\sin^2(\alpha) \leq 0.1$ are shown.

https://doi.org/10.5194/egusphere-2026-2927
Preprint. Discussion started: 31 July 2026

Figure 4. Weighted average of modeled BTs from Figure 3 with different land cover cases weighted according to the average SMOS footprint weights (30% open (non-forested), 67% forested, and 3% water fraction) and adjusted using a free parameter representing a wetland factor: 50% of the open area was modeled as wetland. Periods with snow present are indicated with the black horizontal bars.

480 ### 4.2 Simulating winter SMOS L3 BTs over Umiat site

Previous research has demonstrated the feasibility of retrieving soil temperature below the snow pack from SMOS observations during stable mid-winter conditions (Ortet et al., 2025). This section demonstrates a case study of modeling SMOS observed BTs during winter seasons from one of the sites appearing in (Ortet et al., 2025), assuming stable winter conditions and focusing on the temperature response of modeled and observed BTs. The study site is the U.S. Geological Survey (USGS)

https://doi.org/10.5194/egusphere-2026-2927
Preprint. Discussion started: 31 July 2026

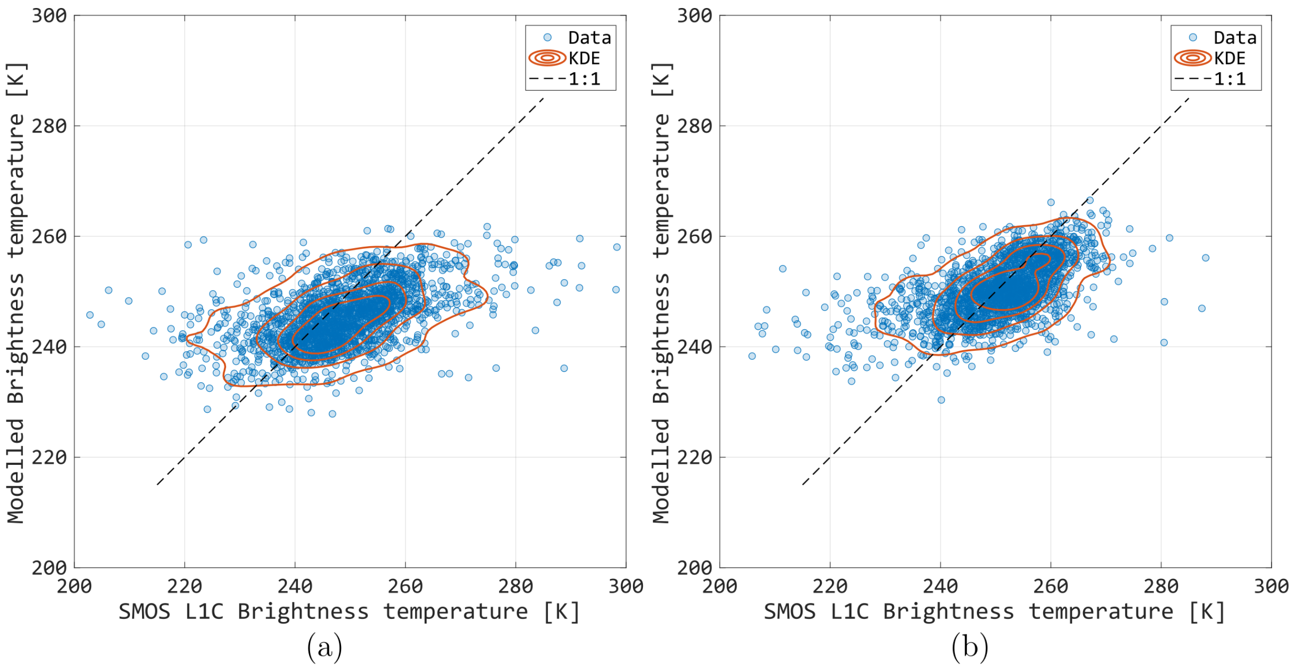

Figure 5. Scatter plots comparing the observed SMOS L1C and modeled average BTs at satellite reference frame linear polarizations X (a panel) and Y (b panel) from the Sodankylä region at the observation angle $\theta = (40 \pm 2.5)°$. All rotation angles α present in the data are shown.

Polarization	N	MD	SDD	R
X	1901	3.2 K	9.5 K	0.49
Y	1873	0.2 K	7.9 K	0.58
X&Y	3774	1.7 K	8.9 K	0.52

Table 3. Number of samples (N), sample mean difference (MD), standard deviation of the difference (SDD) and correlation coefficient (R) corresponding to Figure 5.

Umiat site (Urban and Clow), located in Alaska, USA. A time series of SMOS L3 BTs was extracted for the Umiat grid cell from 2010 to 2019. The corresponding modeled BTs were simulated using the GS model scenario (see Section 3).

In situ measurements continuously collected at the Umiat site were used to parameterize the ground and snow layers. In situ data included air temperature at 2 m above ground, snow depth, and ground temperature at 5 cm depth. The permittivity of frozen soil was assumed as a constant $\varepsilon_\mathrm{g} = 4 + \mathrm{i}0.1$, and the roughness parameters of the ground–snow interface were assumed as $H_\mathrm{g} = 0.8$ and $Q_\mathrm{g} = N_\mathrm{H,g} = N_\mathrm{V,g} = 0$.

While in situ snow depth was used, snow density was assumed as constant with $\rho_\mathrm{s} = 300$ kg m^{-3} and the snowpack was considered dry, i.e., $m_\mathrm{s} = 0$ m^3/m^3. Furthermore, the Umiat region cell was modeled as homogeneous, neglecting vegetation,

https://doi.org/10.5194/egusphere-2026-2927
Preprint. Discussion started: 31 July 2026

water bodies, and heterogeneity in soil or snow properties. The areal fraction of water bodies evaluated from a land cover data was approximately 2%, but during winter, the BT contrast between frozen water bodies and snow-covered soil is smaller than in summer, justifying the omission of radiative effects of water bodies on the simulated BTs representing SMOS observations for the Umiat grid cell.

Figure 6 compares the angular profiles of SMOS L3 and modeled BTs, averaged over the 10 winter periods (January–April) of the study period. The scatter plot in Figure 7 compares individual SMOS L3 and modeled BTs from the January–April 2016 winter period. Both figures demonstrate overall good agreement between observations and the model. Two notable discrepancies are apparent from Figure 7: (i) greater variability in SMOS L3 BTs compared to the modeled values, and (ii) differences between observed and modeled BTs at horizontal polarization for the nadir angle $\theta = 60°$.

The first discrepancy can be attributed to SMOS instrumental noise and geophysical variability, as in situ measurements at a single site may not fully capture the natural heterogeneity present at the Umiat grid cell. A likely contributing factor to the second discrepancy arises from reduced SMOS data quality at large observation angles and from modeling limitations related to the angular response of ground–snow roughness, which are neglected by assuming the empirical roughness parameters $N_{\mathrm{H,g}} = N_{\mathrm{V,g}} = 0$.

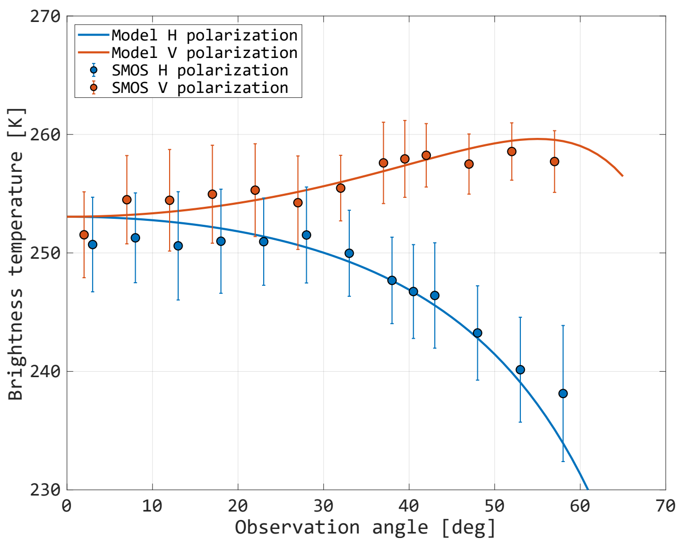

Figure 6. Averaged SMOS L3 and modeled BT angular profiles for the 10 winter periods (January to April) from 2010 to 2019. Markers and error bars show the mean and standard deviations of the SMOS L3 data, respectively.

4.3 SMAP use case from SMAPVEX19-22 Massachusetts site

L-band BTs were modeled for the SMAPVEX19-22 site in Massachusetts (Colliander et al., 2025) and compared with corresponding BTs measured by SMAP. The following in situ measurements available for the Massachusetts site are relevant here: stations with sensors measuring three layers of ground permittivity and temperature, air temperatures, and zenith-looking

https://doi.org/10.5194/egusphere-2026-2927
Preprint. Discussion started: 31 July 2026

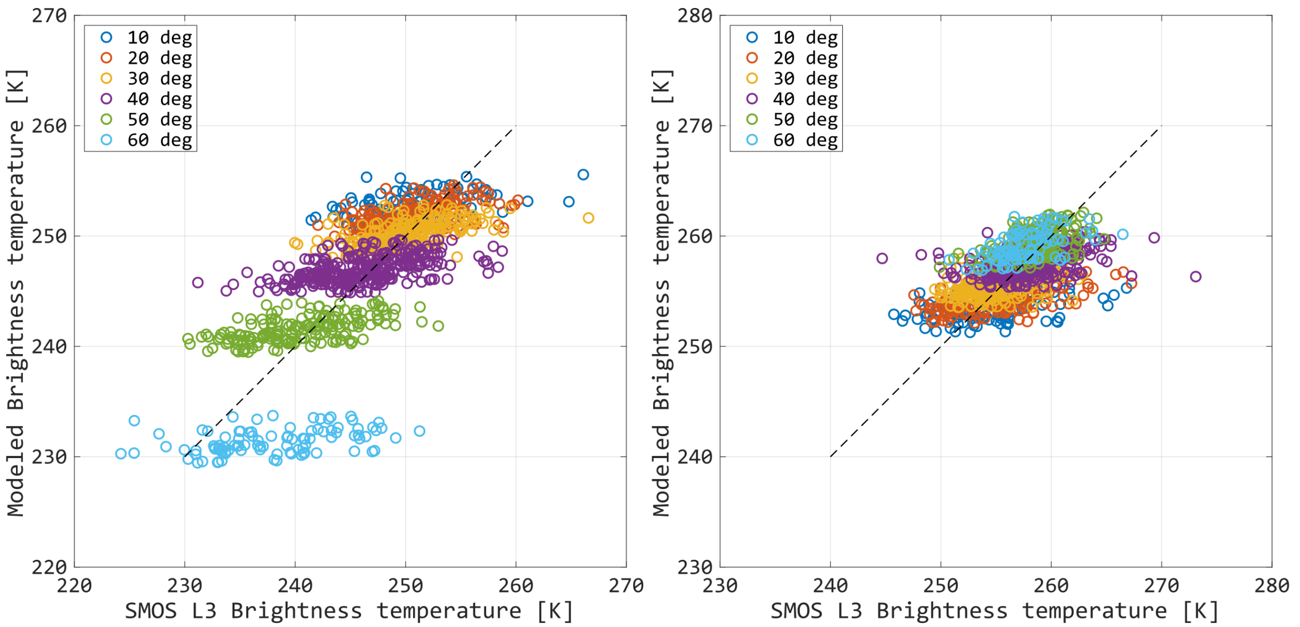

(a) (b)

Figure 7. Scatter plot comparing the observed SMOS L3 and the modeled BTs for horizontal (a panel) and vertical (b panel) polarizations for the winter season from January to April 2016. The sample mean difference, the standard deviation of difference, and the correlation coefficient are 0.2 K, 4.5 K, and 0.73 for horizontal polarization, and -0.1 K, 3.0 K, and 0.56 for vertical polarization. The number of samples was 1107.

cameras to determine plant area index (PAI; (Wohlfahrt et al., 2001)). The PAI time-series was used to separate the foliated and defoliated stages of the trees.

BTs were modeled based on the GGVV model scenario (an extension of the GV scenario model, see Section 3) with the two ground layers and the two vegetation layers parameterized by the mentioned in situ measurements. The parameters defining the radiative transfer in these layers were set as follows: Permittivity $\varepsilon_{\mathrm{g,deep}}$ and temperature $T_{\mathrm{g,deep}}$ of the deeper ground layer were obtained from a horizontally installed in situ sensor at a depth of 5 cm. The permittivity $\varepsilon_{\mathrm{g,surf}}$ of the surface layer was taken from the sensor installed vertically from the surface, but the temperature $T_{\mathrm{g,surf}}$ of the surface layer was also taken from the sensor at 5 cm depth, because the temperature measured by the vertically installed sensor corresponds more to the skin temperature than the near-surface soil temperature, since the thermistor is at the base of the sensor. The imaginary part of the ground surface layer's permittivity was solved by converting the real part measured by the sensor at 50 MHz to soil moisture, which was then converted to the imaginary part at 1.4 GHz using the Mironov 2019 model (Mironov et al., 2020). This approach was adopted because the imaginary part measured at 50 MHz is expected to differ substantially from its value at 1.4 GHz due to relaxation phenomena such as the Maxwell–Wagner effect (Santamarina et al., 2001), which are particularly pronounced in fine-textured soils with high specific surface areas as found in soils with high organic matter and clay contents.

https://doi.org/10.5194/egusphere-2026-2927
Preprint. Discussion started: 31 July 2026

The radiative transfer parameters of the two vegetation layers in the employed GGVV model scenario were defined so that the lower layer represents the woody parts of the trees (stems and branches), and the upper layer represents the foliage. The vertically installed soil sensor (skin temperature) was used to represent the temperature of the vegetation's woody part. The choice was between air temperature, one of the soil temperatures, or their combination. Even though many studies use air temperature to represent vegetation temperature, it exhibits large swings and may not reflect the more slowly responding temperature of the woody vegetation parts of the trees, but rather the foliage; therefore, it was used to represent foliage temperature.

The set of ground interface roughness parameters were assumed as $Q_\mathrm{g} = N_\mathrm{H,g} = N_\mathrm{V,g} = 0$, while the H_g and the scattering albedo $\omega_\mathrm{v,low}$ of the lower vegetation layer, including the woody parts, were tuned during the defoliated stage of the trees. The resulting $\omega_\mathrm{v,low}$ tuned for the defoliated stage was also applied during the foliated stage. The scattering albedo of the upper layer, $\omega_\mathrm{v,up}$, mostly including vegetation constituents smaller than the observation wavelength, was assumed as $\omega_\mathrm{v,up} = 0$. The VOD τ_v was simulated using the L-VOD model (Schwank et al., 2021, 2024), evaluated for the in situ measured biomass of the vegetation and its time dependent in situ temperature T_v.

Before performing the 2S-MEM forward simulation of BTs, the permittivities and temperatures were averaged to estimate the values representing the SMAP footprint area. Figure 8 shows the time series of the observed and modeled BT using two models, one with leaves modeled as described above, and other without. The modeled BT time series are smoothed for visual purposes using a Gaussian filter with window size of $\sigma = 3$ days. Figure 8 shows improved agreement between the model and observations when leaves are modeled using the two vegetation layers. During the defoliated stage the two models agree.

Figure 9 shows scatter plots of observed versus the modeled BT. Black markers show the defoliated instances, where the two models agree. Blue and orange markers show the two models. An improvement in terms of the mean difference between the modeled and SMAP measured BTs was observed: at horizontal polarization from 3.6 K without leaves to -0.3 K when the leaves were modeled, and similarly for vertical polarization mean difference dropped from 3.0 K to -0.1 K when considering leaves. Both the sample standard deviation of difference and correlation coefficient improved when the leaves were modeled, but not significantly.

5 Discussion

The two-stream radiative (2S) transfer modeling has two intrinsic differences to the zeroth order $\tau - \omega$ approach:

1. The 2S approach is not limited in terms of number of layers, while the nominal $\tau - \omega$ is restricted to a soil substrate covered by a single vegetation layer.

2. Volume scattering is modeled differently between the two; in $\tau - \omega$ the scattered radiation vanishes, while in 2S it is transferred into the opposing stream of radiation.

The first difference is relevant in modeling more complex layered systems where the $\tau - \omega$ setting is not sufficient. For example, such instances appear related to soil freezing, presence of snow (in particular snow melting), and dense forest. The second difference is most relevant in case of dense vegetation and forest, where the volume scattering plays a significant role at L-

https://doi.org/10.5194/egusphere-2026-2927
Preprint. Discussion started: 31 July 2026

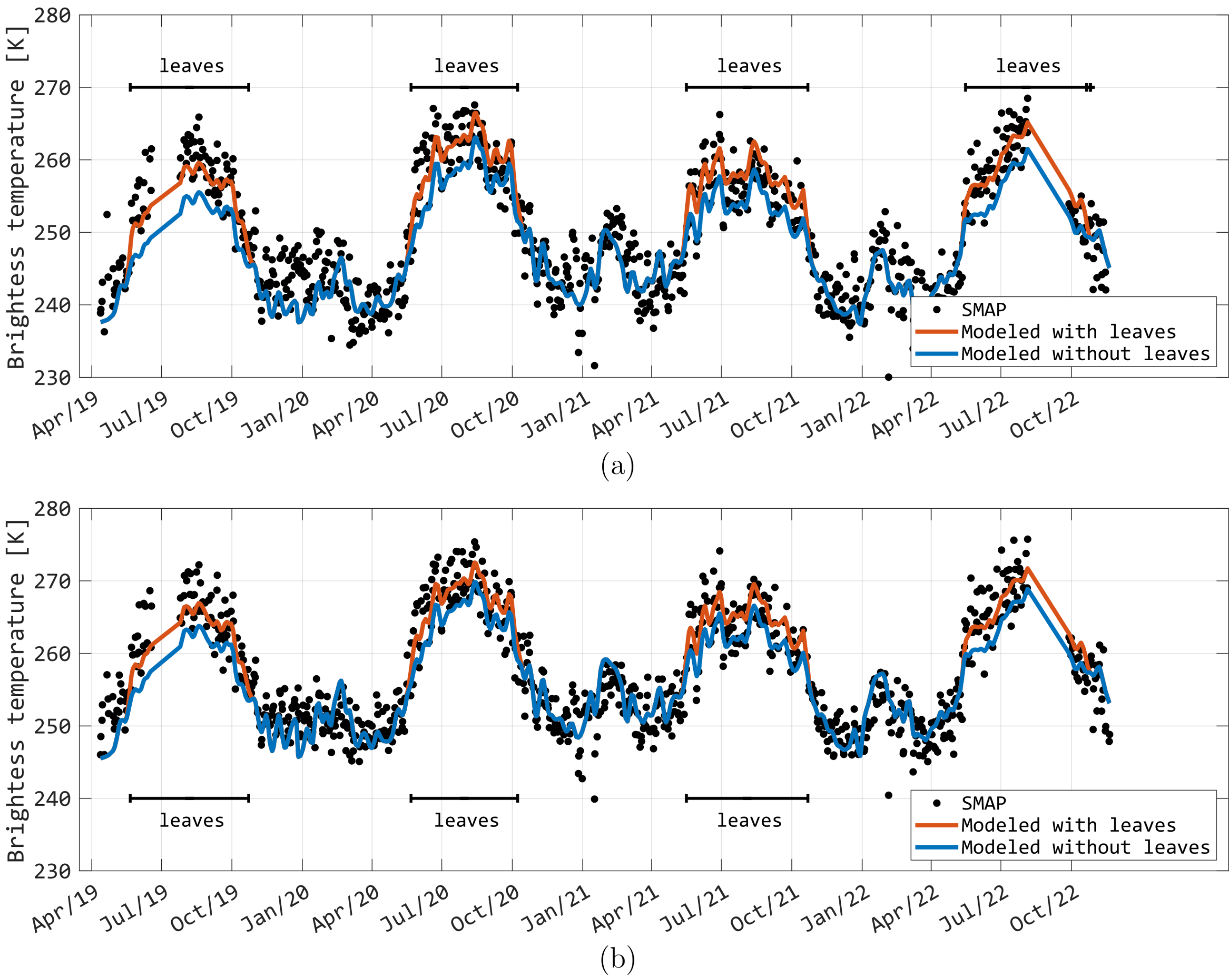

Figure 8. SMAP and modeled BT at H-polarization (a) and V-polarization (b) over the Massachusetts site. In both panels, two modeling choices are shown: i) the upper vegetation layer (foliage) with the tuned VOD and ii) zero VOD (no leaves). Option i) was applied when the leaves were present based on the PAI estimates, and consequently the two models agree when leaves are not present. The modeled BTs are smoothed with Gaussian filter and $\sigma = 3$ days window size for visual purposes.

band. The two models agree in a trivial case with only a soil substrate and an atmosphere layer. Addition of a scattering vegetation layer creates a disagreement between the models due to the different scattering mechanisms. Without scattering, the models agree. See (Schwank et al., 2018) for an analysis of the differences of the 2S and $\tau-\omega$ modeling for vegetation.

Results in Section 4.1 demonstrated the performance of the 2S L-MEM on a heterogeneous Northern boreal site. This case study demonstrated the need for a multi-layer model in order to have a consistent modeled BTs across the season, including the presence of snow. The model was able to capture both the absolute level and dynamics of the observed BT time series

https://doi.org/10.5194/egusphere-2026-2927
Preprint. Discussion started: 31 July 2026

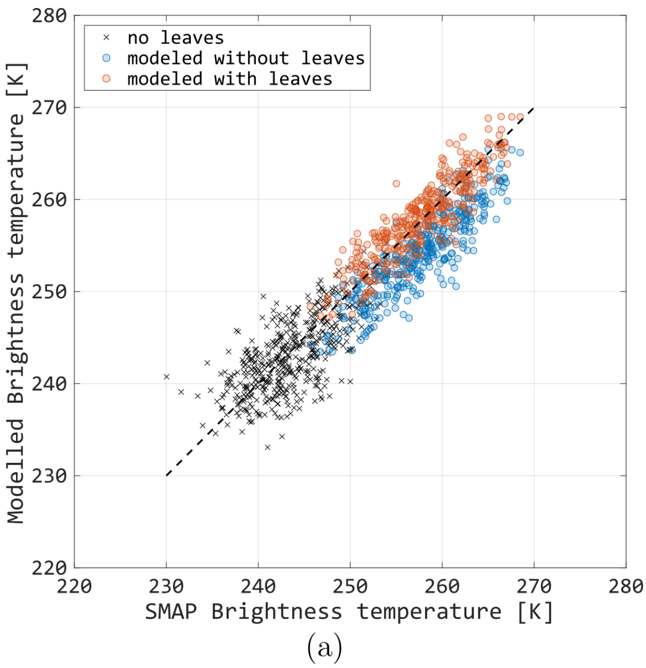

Figure 9. Observed versus modeled BT for H-polarization (a) and V-polarization (b) with the two foliage modeling options. Black markers show the periods without leaves, when the two models agree, orange show cases where leaves were modeled and blue markers where they were omitted from the model during the periods with leaves present. Modeling leaves improved the sample mean difference from 3.6 K to -0.3 K for H polarization and 3.0 K to -0.1 K for V polarization. Both the sample standard deviation of difference and correlation coefficient improved in for both polarizations, but not significantly.

(Figure 4), although the standard deviation of the difference between the observed and modeled BT was larger (~ 9 K) than what is the expected uncertainty of the SMOS observations (~ 4 K). Two possible sources of modeling error are: First, presence and amount of liquid water in the snow pack. Second: wetlands were modeled using a simple soil substrate. However, due to organic top layer and variable water level using multiple layers to model wetlands might be needed.

Section 4.2 demonstrated the use of the 2S L-MEM on an arctic tundra site located in Alaska, focusing on the stable winter conditions. This was motivated by a previous study (Ortet et al., 2025), which demonstrated the feasibility of retrieving soil temperature below the snow pack is such conditions. The results of Section 4.2 showed that on average, the modeled BT were in good agreement with the observed values throughout the study period (Figure 6). The study site included only one in situ station, introducing large uncertainty in terms of the spatial heterogeneity and its effects to the BT.

Section 4.3 showed a comparison of the modeled BTs to the ones measured by the SMAP satellite over one of its core validation sites with extensive in situ data. This case study demonstrated the use of the multi-layer capability using two soil layers together and two vegetation layers. In particular, an explicit modeling of the forest foliage improved the agreement of the modeled and SMAP BTs (Figures 8 and 9). In this case study the spatial heterogeneity of the soil permittivity was omitted by

https://doi.org/10.5194/egusphere-2026-2927
Preprint. Discussion started: 31 July 2026

using an average permittivity value. This was not seen to produce noticeable errors. This is likely due to relative homogeneity of the site in terms of its soil permittivity.

As discussed in the Section 3.2, the satellite observed BT is modeled as an integral of the local observation operator, weighted by the antenna pattern, over the observation area (Eq. (17)). From this viewpoint, the modeling errors can be divided into two parts:

1. Errors related to the spatial heterogeneity, originating from assumptions imposed on the spatial fields of the geophysical variables and land cover.

2. Errors and uncertainties included in the local observation operator, i.e. in the scenario models.

The errors included in the first item are more explicit, while some of the errors and uncertainties related in the second item are more implicit and difficult to address.

In the present study, the spatial heterogeneity was partly considered in the case study of Section 4.1 by modeling BT separately from multiple spatially distributed stations, and then averaging them into a BT representative of the satellite-observed value. However, spatially homogeneous VOD value was used for the forested sites across the region. On the other hand, case studies in Sections 4.2 and 4.3 omitted the spatial heterogeneity all together.

Errors and uncertainties related to the local observation operator include uncertainties in the underlying physics (e.g., reflectivity of a rough surface and volume scattering within a complex vegetation structure) which have been simplified into parameters such as H_{g} and ω_{v}. These are usually not known from any in situ measurements, and have to be either calibrated by matching the observed and modeled BT, or set manually. In this study, we took the latter approach in order to have relatively simple demonstration of the 2S L-MEM, however, at the cost of introducing modeling errors.

Also structural model errors are present. For example, in the case study presented in Section 4.1, a more complex multi-layer model for wetlands should be considered. In Sections 4.2 a single soil substrate was used with in situ data from 5 cm depth. In particular, during winter with deeply frozen soil a multiple soil layers could improve the modeling. In both of the case studies a homogeneous and dry snow pack was assumed. In reality a multi-layer model representing natural density gradient and wet snow layers should be considered.

The 2S radiative transfer is a special case of a more general N-stream radiative transfer, and thus introduces errors via the made simplification to the radiative transfer. Another source of uncertainty are the dielectric functions used to translate the layer's geophysical properties into effective dielectric properties. The L-VOD model has conceptually similar role of converting the geophysical properties of the forest layer into effective radiative transfer parameter, VOD. These functions are often semi-empirical which depend on medium's structural characteristics (e.g., soil composition or forest structural parameters) and other empirical regression coefficients. Consequently, the dielectric functions contain their own errors and uncertainties, on the one hand related to their inherent incomplete physics or empirical approach, and on the other hand, uncertain parameterization. These errors propagate to the modeled BTs.

https://doi.org/10.5194/egusphere-2026-2927
Preprint. Discussion started: 31 July 2026

6 Conclusions

This paper reviewed a previously established modeling framework for L-band remote sensing, and described its use to model satellite observations. Three case studies were presented, demonstrating the models performance in typical scenarios requiring or benefiting from multi-layer approach, which is not possible in the contemporary $\tau - \omega$ modeling approach. In particular, the 2S L-MEM is able to model natural targets outside the scope of the $\tau - \omega$, such as freezing-soil, multi-layer snow pack, and dense multi-layer vegetation. Modeling the satellite observed BT from the spatially distributed in situ data is a complex task independent of the used model. First, the in situ data is rarely, if ever, sufficient and part of the required model inputs have to be either manually set or calibrated based on the observations. The sparsely distributed in situ sites provide only partial information on the spatial heterogeneity of the observed area. While these uncertainties were partly addressed, more focused studies are needed in order to have a better understanding and characterization of the modeling errors, in particular over different land cover types.

Code and data availability. The 2S L-MEM source code, together with a runnable example that reproduces a representative simulation, is archived on Zenodo under https://doi.org/10.5281/zenodo.20283043 (Holmberg et al., 2026). The satellite and reanalysis datasets used in the three case studies are publicly available from their respective archives: SMOS Level-1 products including L1C at https://doi.org/10.57780/SM1-e20cf57 (European Space Agency, 2009); CATDS-PDC L3TB brightness temperatures at https://doi.org/10.12770/6294e08c-baec-4282-a251-33fee22ec67f (Al Bitar et al., 2017); SMAP Enhanced L2 Radiometer Half-Orbit 9 km EASE-Grid Soil Moisture, Version 6, https://doi.org/10.5067/BN36FXOMMC4C (ONeill et al., 2023); and ERA5-Land hourly data at https://doi.org/10.24381/cds.e2161bac (Muñoz Sabater, 2019). The used in situ data used in Sections 4.1, 4.2, and 4.3 are available from https://litdb.fmi.fi/index.php, (Ikonen et al., 2016), https://doi.org/10.5066/F7VX0FGB, (Urban and Clow), and https://doi.org/10.5067/3LXL78PSKVXQ, (Cosh et al., 2020) and https://doi.org/10.5067/14BX4UOPEVRX, (Kraatz et al., 2025), respectively. The application-specific processing scripts that combine the model code with these inputs to produce the case-study results were developed across several authors in the course of the study and have not yet been consolidated into a publishable software release; they are available from the corresponding author on reasonable request.

Appendix A: Derivation of the layer coefficients

Consider a homogeneous layer with thickness d, temperature T, and absorption and scattering coefficients κ_a and κ_s, respectively. Denote the upwards radiating field at a local propagation angle θ as a function of depth z by $y(z)$ and similarly the downwards radiating field by $a(z)$. With respect to these two, the radiative transfer equation under the two-stream assumption is written as a pair of linear first order differential equations

$$\begin{aligned} \mu y'(z) + \kappa_\mathrm{e} y(z) &= \kappa_\mathrm{a} T + \kappa_\mathrm{s} a(z) \\ -\mu a'(z) + \kappa_\mathrm{e} a(z) &= \kappa_\mathrm{a} T + \kappa_\mathrm{s} y(z), \end{aligned} \tag{A1}$$

https://doi.org/10.5194/egusphere-2026-2927
Preprint. Discussion started: 31 July 2026

where $\mu = \cos\theta$ and $\kappa_\mathrm{e} = \kappa_\mathrm{a} + \kappa_\mathrm{s}$ is the extinction coefficient. Defining new functions $\tilde{y} = y - T$, $\tilde{a} = a - T$ and making the change of variable $s = \kappa_\mathrm{e} z/\mu$ results in

$$\begin{aligned} \tilde{y}'(s) + \tilde{y}(s) &= \omega\tilde{a}(s) \\ -\tilde{a}'(s) + \tilde{a}(s) &= \omega\tilde{y}(s). \end{aligned} \tag{A2}$$

The general solution is

$$\begin{aligned} \tilde{y}(s) &= Ae^{ks} + Be^{-ks} \\ \tilde{a}(s) &= A'e^{ks} + B'e^{-ks}, \end{aligned} \tag{A3}$$

with $k = (1-\omega^2)^{1/2}$, $A' = A(1+k)/\omega$, $B' = B(1-k)/\omega$, and the coefficients A and B are the free constants to be determined from the boundary conditions. Denote $\alpha = (1+k)/\omega$ and $\beta = (1-k)/\omega$, and noting that $\alpha\beta = 1$, Eq. (A3) can be written as

$$\begin{aligned} \tilde{y}(s) &= Ae^{ks} + Be^{-ks} \\ \tilde{a}(s) &= \alpha Ae^{ks} + \frac{B}{\alpha}e^{-ks}. \end{aligned} \tag{A4}$$

Inserting $s = 0$ (bottom interface) into the first and $s = S$ (top interface) into the second equation in (A4), and considering the inwards radiating fields $\tilde{y}_0 = \tilde{y}(0)$ and $\tilde{a}_1 = \tilde{a}(S)$ as fixed boundary conditions yields

$$\begin{aligned} \tilde{y}_0 &= A + B \\ \tilde{a}_1 &= \frac{1}{rt}A + rtB, \end{aligned} \tag{A5}$$

where $t = e^{-kS}$ and $r = 1/\alpha$. Solving Equations (A5) yields expressions for A and B in terms of the boundary conditions

$$A = -\frac{r^2t^2}{1-r^2t^2}\tilde{y}_0 + \frac{rt}{1-r^2t^2}\tilde{a}_1, \quad B = \frac{1}{1-r^2t^2}\tilde{y}_0 - \frac{rt}{1-r^2t^2}\tilde{a}_1. \tag{A6}$$

Inserting these back to Eq. (A4) gives first for $\tilde{y}_1 = \tilde{y}(S)$

$$\tilde{y}_1 = \tilde{y}_0 t\frac{1-r^2}{1-r^2t^2} + \tilde{a}_1 r\frac{1-t^2}{1-r^2t^2}, \tag{A7}$$

and similarly for $\tilde{a}_0 = \tilde{a}(0)$

$$\tilde{a}_0 = \tilde{y}_0 r\frac{1-t^2}{1-r^2t^2} + \tilde{a}_1 t\frac{1-r^2}{1-r^2t^2}. \tag{A8}$$

Now, returning to the original variables $y = \tilde{y} + T$ and $a = \tilde{a} + T$ gives the volume equations linking the four radiation quantities at the bottom and top interfaces of the layer

$$\begin{aligned} y_1 &= w_1y_0 + w_2a_1 + w_3T \\ a_0 &= w_2y_0 + w_1a_1 + w_3T \end{aligned} \tag{A9}$$

where

$$w_1 = t\frac{1-r^2}{1-r^2t^2}, \quad w_2 = r\frac{1-t^2}{1-r^2t^2}, \quad w_3 = 1 - w_1 - w_2. \tag{A10}$$

https://doi.org/10.5194/egusphere-2026-2927
Preprint. Discussion started: 31 July 2026

Appendix B: Computing the satellite footprint's radiometric weights

The usual values given in the satellite data that describe the footprint size and shape are the minor and major axis and the azimuth angle (measured clockwise from North). Denote these three by W_a, W_b, and α, respectively.

Consider first a local cartesian plane projection where $r = [x,y]^\top$ and $r = r_0$ is the footprint center coordinate. Considering a baseline shape $G_0(r)$, the footprint density pattern can be modeled as

$$G(r) = \frac{1}{z} G_0\left(S_{a,b}^{-1} R_\phi^{-1}(r - r_0)\right) \tag{B1}$$

where z is a normalizing constant and

$$R_\phi = \begin{bmatrix} \cos\phi & \sin\phi \\ -\sin\phi & \cos\phi \end{bmatrix}, \quad S_{a,b} = \begin{bmatrix} a & 0 \\ 0 & b \end{bmatrix}. \tag{B2}$$

are the clockwise rotation and scaling matrices. For a standard Gaussian $G_0 \propto \exp(-\frac{1}{2}\|r\|^2)$ this results into $G(r)$ being a Gaussian density with covariance $\Sigma = R_\phi S S^\top R_\phi^\top$ and mean r_0. The values W_a and W_b provided in the satellite data often are the full width -3 dB values of the footprint density with respect to its peak value. Assuming Gaussian density pattern, the standard deviation values a and b of the scaling matrix are related to the W_a and W_b by

$$a = \frac{W_a}{2\sqrt{2\log 2}}, \quad b = \frac{W_b}{2\sqrt{2\log 2}} \tag{B3}$$

This relation is fully dependent on the assumed shape of the footprint density pattern.

If the land cover data $S(r)$ is available on a local Cartesian plane projection (e.g. UTM), then the footprint radiometric weights for different land cover classes are given by the integrals

$$w_s = \int\limits_{S(r)=s} G(r)\mathrm{d}r, \tag{B4}$$

to which a practical approximation is to compute the following sums over the grid cells r_{ij} with land cover class s

$$\tilde{w}_s = \sum_{S(r_{ij})=s} G(r_{ij}) a_{ij}, \tag{B5}$$

where a_{ij} denotes the area of the grid cell. The coefficients w_s are obtained by normalizing $\tilde{w}_s$ over s.

However, often the land cover data is given in geographical coordinates, i.e. $\ell = [\lambda, \phi]^\top$. A practical approximation is to consider a local Cartesian plane centered at the footprint center ℓ_0 with coordinates $u = [u_x, u_y]^\top$. Linearization

$$\begin{aligned} \lambda - \lambda_0 &\approx \frac{u_x}{R\cos\phi_0} \\ \phi - \phi_0 &\approx \frac{u_y}{R} \end{aligned} \tag{B6}$$

can be used to approximate the footprint density pattern in the λ coordinates

$$G_{\mathrm{geo}}(\ell) = \frac{1}{z} G_{\mathrm{cart}}(A^{-1}(\ell - \ell_0)), \quad A = \begin{bmatrix} \frac{1}{R\cos\phi_0} & 0 \\ 0 & \frac{1}{R} \end{bmatrix} \tag{B7}$$

Here R is the Earth's radius in the same units as u_x and u_y and longitude λ and latitude ϕ are in radians. If the density pattern G_{cart} in the Cartesian coordinates is a Gaussian with mean $u = 0$ (by the definition of the local coordinate system) and covariance $\Sigma_{\mathrm{cart}} = R_\phi S S^\top R_\phi^\top$, then the approximate pattern G_{geo} is Gaussian with mean ℓ_0 and covariance $\Sigma_{\mathrm{geo}} = A \Sigma_{\mathrm{cart}} A^\top$. The land cover weights are then estimated similar to Eq. (B5).

Author contributions. MH proposed the study, implemented the current version of the model code, building on earlier implementations by MS and JL. MH led the writing of the first draft with contributions from all co-authors. MS developed the original modelling concept. MH, AC and JO each applied the model to one of the case studies, performed the corresponding investigation and analysis, and produced the associated results. PR provided data used in the study. JL, KR, and YK contributed to funding acquisition. All co-authors provided scientific feedback and contributed to writing and editing the manuscript.

Competing interests. Authors declare no competing interests.

Acknowledgements. Authors would like to thank Nemesio Rodriguez-Fernandez for reviewing and providing valuable feedback on the manuscript. The authors used Anthropic's Claude to assist with English language editing of the manuscript. All scientific content and conclusions are the authors' own. This work was funded by the European Space Agency project SMOS ESL2020+ (ESA contract no. 4000130567/20/I-BG), the Research Council of Finland Academy Research Fellowship project EMonSoil (grant no. 364034), and the Research Council of Finland Flagship programs Advanced Mathematics for Sensing Imaging and Modelling (FAME; grant no. 359196).

https://doi.org/10.5194/egusphere-2026-2927
Preprint. Discussion started: 31 July 2026

References

Al Bitar, A., Mialon, A., Kerr, Y., Cabot, F., Richaume, P., Jacquette, E., Quesney, A., Mahmoodi, A., Tarot, S., Parrens, M., Al-Yaari, A., Pellarin, T., Rodriguez-Fernandez, N., and Wigneron, J.-P.: The Global SMOS Level 3 Daily Soil Moisture and Brightness Temperature Maps, Earth System Science Data, 9, 293–315, https://doi.org/10.5194/essd-9-293-2017, 2017.

Bojinski, S., Verstraete, M., Peterson, T. C., Richter, C., Simmons, A., and Zemp, M.: The concept of essential climate variables in support of climate research, applications, and policy, Bulletin of the American Meteorological Society, 95, 1431–1443, 2014.

Boutin, J., Reul, N., Köhler, J., Martin, A., Catany, R., Guimbard, S., Rouffi, F., Vergely, J.-L., Arias, M., Chakroun, M., et al.: Satellite-based sea surface salinity designed for ocean and climate studies, Journal of Geophysical Research: Oceans, 126, e2021JC017 676, 2021.

Chen, K. and Tan, S.: A Multiple-Scattering Microwave Radiative Transfer Model for Land Emission With Vertically Heterogeneous Vegetation Coverage, IEEE TRANSACTIONS ON GEOSCIENCE AND REMOTE SENSING, 62, https://doi.org/10.1109/TGRS.2024.3411557, 2024.

Choudhury, B., Schmugge, T., Newton, R., and Chang, A.: Effect of Surface Roughness on the Microwave Emission From Soils, Journal of Geophysical Research, 84, 5699–5706, https://doi.org/10.1029/JC084iC09p05699, 1979.

Colliander, A., Cosh, M. H., Bourgeau-Chavez, L., Kelly, V., Kraatz, S., Siqueira, P., Walker, V. A., Chen, X., Roy, A., Lakhankar, T., et al.: SMAP validation experiment 2019-2022 (SMAPVEX19-22): Field campaign to improve soil moisture and vegetation optical depth retrievals in temperate forests, IEEE Journal of Selected Topics in Applied Earth Observations and Remote Sensing, 2025.

Colliander, A., Schwank, M., Zhou, Y., Kurum, M., Vittucci, C., Tsang, L., Roy, A., and Berg, A.: A review of forward modelling and retrieval approaches for forest soil moisture and vegetation optical depth using L-band radiometry, REMOTE SENSING OF ENVIRONMENT, 334, https://doi.org/10.1016/j.rse.2025.115158, 2026.

Cosh, M., Kraatz, S., and Colliander, A.: SMAPVEX19-22 Massachusetts Temporary Soil Moisture Network, Version 1, https://doi.org/10.5067/3LXL78PSKVXQ, 2020.

Dobson, M. C., Ulaby, F. T., Hallikainen, M. T., and Elrayes, M. A.: Microwave Dielectric Behavior of Wet Soil 2: Dielectric Mixing Models, IEEE TRANSACTIONS ON GEOSCIENCE AND REMOTE SENSING, 23, 35–46, https://doi.org/10.1109/TGRS.1985.289498, 1985.

Entekhabi, D., Njoku, E. G., O'Neill, P. E., Kellogg, K. H., Crow, W. T., Edelstein, W. N., Entin, J. K., Goodman, S. D., Jackson, T. J., Johnson, J., Kimball, J., Piepmeier, J. R., Koster, R. D., Martin, N., McDonald, K. C., Moghaddam, M., Moran, S., Reichle, R., Shi, J. C., Spencer, M. W., Thurman, S. W., Tsang, L., and Van Zyl, J.: The Soil Moisture Active Passive (SMAP) Mission, PROCEEDINGS OF THE IEEE, 98, 704–716, https://doi.org/10.1109/JPROC.2010.2043918, 2010.

Entekhabi, D., Yueh, S., Bindlish, R., Garcia, M., Entin, J., Colliander, A., Chaubell, M., Crow, W., Dunbar, R., Herwehe, L., Kimball, J., Mohammed, P., Reichle, R., Chung, N., Dinnat, E., Huang, H., Khalsa, S., Levine, D., Misra, S., Pashaian, L., Peng, J., Piepmeier, J., Rodriguez-Alvarez, N., Wang, T., Xu, X., Ahmadisharaf, E., Bras, R., Chen, C., Chen, A., Das, N., Ebtehaj, A., Frankenberg, C., Green, J., Hornbuckle, B., Keenan, T., Kolassa, J., Konings, A., Koster, R., Kumar, S., Kurum, M., Morris, M., Negron-Juarez, R., Petty, A., Potter, C., Salvucci, G., Tsang, L., and Zhao, M.: The NASA Soil Moisture Active Passive (SMAP) Earth Observation Satellite Mission, manuscript under review at Proceedings of the IEEE, 2025.

European Space Agency: Soil Moisture and Ocean Salinity (SMOS) Level 1C Brightness Temperature Data, https://earth.esa.int/eogateway/catalog/smos-science-products, 2009.

Fan, L., Wigneron, J.-P., Ciais, P., Chave, J., Brandt, M., Fensholt, R., Saatchi, S. S., Bastos, A., Al-Yaari, A. ad Hufkens, K., Qin, Y., Xiao, X., Chen, C., Myneni, R. B., Fernandez-Moran, R., Mialon, A., Rodriguez-Fernandez, N., Kerr, Y., Tian, F., and Peñuelas, J.: Satellite-observed pantropical carbon dynamics, Nature plants, 5, 944–951, 2019.

Fernandez-Moran, R., Al-Yaari, A., Mialon, A., Mahmoodi, A., Al Bitar, A., De lannoy, G., Rodriguez-Fernandez, N., Lopez-Baeza, E., Kerr, Y., and Wigneron, J.-P.: SMOS-IC: An Alternative SMOS Soil Moisture and Vegetation Optical Depth Product, REMOTE SENSING, 9, https://doi.org/10.3390/rs9050457, 2017.

Ferrazzoli, P., Guerriero, L., and Wigneron, J.-P.: Simulating L-band emission of forests in view of future satellite applications, IEEE Transactions on Geoscience and Remote Sensing, 40, 2700–2708, 2003.

Hallikainen, M., Ulaby, F., Dobson, M., and El-Rayes, M.: Dielectric measurements of soils in the 3 to 37 GHz band between-50° C and 23° C, ESA IGARSS 84. Remote Sensing: From Res. Towards Operational Use,, 1, 1984.

Hallikainen, M. T., Ulaby, F. T., Dobson, M. C., Elrayes, M. A., and Wu, L. K.: Microwave Dielectric Behavior Of Wet Soil 1: Empirical-Models And Experimental-Observations, IEEE TRANSACTIONS ON GEOSCIENCE AND REMOTE SENSING, 23, 25–34, https://doi.org/10.1109/TGRS.1985.289497, 1985.

Holmberg, M., Lemmetyinen, J., Schwank, M., Kontu, A., Rautiainen, K., Merkouriadi, I., and Tamminen, J.: Retrieval of Ground, Snow, and Forest Parameters From Space Borne Passive L Band Observations. A Case Study Over Sodankylä, Finland, Remote Sensing of Environment, 306, https://doi.org/10.1016/j.rse.2024.114143, 2024.

Holmberg, M., Lemmetyinen, J., Richaume, P., Colliander, A., Kontu, A., and Tamminen, J.: Bayesian Time Series Approach and Its Application to Retrieve Ground and Vegetation Variables From L-Band Passive Microwave Remote Sensing, IEEE TRANSACTIONS ON GEOSCIENCE AND REMOTE SENSING, 63, https://doi.org/10.1109/TGRS.2025.3585275, 2025.

Holmberg, M., Schwank, M., and Lemmetyinen, J.: Multilayer Emission Model for Passive L-Band Satellite Observations on Land (2S L-MEM), https://doi.org/10.5281/zenodo.20283043, 2026.

Hossan, A., Colliander, A., Schlegel, N.-J., Harper, J., Andrews, L., Kolassa, J., Miller, J. Z., and Cullather, R.: Evaluation of wet snow dielectric mixing models for L-band radiometric measurement of liquid water content in Greenland's percolation zone, CRYOSPHERE, 19, 6077–6102, https://doi.org/10.5194/tc-19-6077-2025, 2025.

Houtz, D., Matzler, C., Naderpour, R., Schwank, M., and Steffen, K.: Quantifying Surface Melt and Liquid Water on the Greenland Ice Sheet using L-band Radiometry, REMOTE SENSING OF ENVIRONMENT, 256, https://doi.org/10.1016/j.rse.2021.112341, 2021.

Ikonen, J., Vehvilainen, J., Rautiainen, K., Smolander, T., Lemmetyinen, J., Bircher, S., and Pulliainen, J.: The Sodankyla In Situ Soil Moisture Observation Network: An Example Application of Esa CCI Soil Moisture Product Evaluation, Geoscientific Instrumentation Methods and Data Systems, 5, 95–108, https://doi.org/10.5194/gi-5-95-2016, 2016.

Ishimaru, A.: Wave Propagation and Scattering in Random Media, Volume 1: Single Scattering and Transport Theory, Academic Press, New York, 1978.

Kerr, Y., Waldteufel, P., Wigneron, J.-P., Delwart, S., Cabot, F., Boutin, J., Escorihuela, M.-J., Font, J., Reul, N., Gruhier, C., Juglea, S., Drinkwater, M., Hahne, A., Martin-Neira, M., and Mecklenburg, S.: The SMOS Mission: New Tool for Monitoring Key Elements of the Global Water Cycle, Proceedings of the IEEE, 98, 666–687, https://doi.org/10.1109/JPROC.2010.2043032, 2010.

Kerr, Y., Waldteufel, P., Richaume, P., Wigneron, J.-P., Ferrazzoli, P., Mahmoodi, A., Al Bitar, A., Cabot, F., Gruhier, C., Juglea, S., Leroux, D., Mialon, A., and Delwart, S.: The SMOS Soil Moisture Retrieval Algorithm, IEEE Transactions on Geoscience and Remote Sensing, 50, 1384–1403, https://doi.org/10.1109/TGRS.2012.2184548, 2012.

https://doi.org/10.5194/egusphere-2026-2927
Preprint. Discussion started: 31 July 2026

Kerr, Y. H. and Njoku, E. G.: A SEMIEMPIRICAL MODEL FOR INTERPRETING MICROWAVE EMISSION FROM SEMIARID LAND SURFACES AS SEEN FROM SPACE, IEEE TRANSACTIONS ON GEOSCIENCE AND REMOTE SENSING, 28, 384–393, https://doi.org/10.1109/36.54364, 1990.

Kerr, Y. H., Waldteufel, P., Richaume, P., Wigneron, J.-P., Ferrazzoli, P., and Gurney, R.: SMOS level 2 processor for soil moisture - Algorithm Theoretical Based Document (ATBD), Tech. Rep. SO-TN-ESL-SM-GS-0001, Issue 3.e, CESBIO, http://www.cesbio.ups-tlse.fr/fr/indexsmos.html, 121 p., 2011.

Kontu, A.: L-Band Observations of Soil and Trees in Freezing/Thawing Conditions, Final Report, Tech. rep., European Space Agency, 2022.

Kraatz, S., Cosh, M. H., Kelly, V., Colliander, A., and Siqueira, P. R.: SMAPVEX19-22 Massachusetts Plant Area Index, Version 1, https://doi.org/10.5067/14BX4UOPEVRX, 2025.

Kumawat, D., Ebtehaj, A., Kumar, S., and Colliander, A.: Deep learning of seasonal peak snow water content of global boreal forest and arctic using spaceborne L-band radiometry, REMOTE SENSING OF ENVIRONMENT, 330, https://doi.org/10.1016/j.rse.2025.114963, 2025a.

Kumawat, D., Ebtehaj, A., Xu, X., Colliander, A., and Kumar, V.: An Autoencoder Architecture for L-Band Passive Microwave Retrieval of Landscape Freeze-Thaw Cycle, IEEE TRANSACTIONS ON GEOSCIENCE AND REMOTE SENSING, 63, https://doi.org/10.1109/TGRS.2025.3530356, 2025b.

Lannoy, G. J. M. D. and Reichle, R. H.: Global Assimilation of Multiangle and Multipolarization SMOS Brightness Temperature Observations into the GEOS-5 Catchment Land Surface Model for Soil Moisture Estimation, Journal of Hydrometeorology, 17, 669–691, https://doi.org/10.1175/JHM-D-15-0037.1, 2016.

Lemmetyinen, J., Schwank, M., Rautiainen, K., Kontu, A., Parkkinen, T., Mätzler, C., Wiesmann, A., Wegmüller, U., Derksen, C., Toose, P., et al.: Snow density and ground permittivity retrieved from L-band radiometry: Application to experimental data, Remote sensing of environment, 180, 377–391, 2016.

Li, X., Al-Yaari, A., Schwank, M., Fan, L., Frappart, F., Swenson, J., and Wigneron, J.-P.: Compared performances of SMOS-IC soil moisture and vegetation optical depth retrievals based on Tau-Omega and Two-Stream microwave emission models, Remote Sensing of Environment, 236, 111 502, 2020.

Martín-Neira, M., Ribó, S., and Martín-Polegre, A.: Polarimetric mode of MIRAS, IEEE Transactions on Geoscience and Remote Sensing, 40, 1755–1768, https://doi.org/10.1109/TGRS.2002.802489, 2002.

Mätzler, C.: Applications of SMOS over terrestrial ice and snow, in: Proceedings of the 3rd SMOS Workshop, DLR, Oberpfaffenhofen, Germany, pp. 10–12, 2001.

Mialon, A., Rodríguez-Fernández, N. J., Santoro, M., Saatchi, S., Mermoz, S., Bousquet, E., and Kerr, Y. H.: Evaluation of the sensitivity of SMOS L-VOD to forest above-ground biomass at global scale, Remote Sensing, 12, 1450, 2020.

Mironov, V., Karavayskiy, A. Y., Lukin, Y. I., and Molostov, I. P.: A dielectric model of thawed and frozen Arctic soils considering frequency, temperature, texture and dry density, International journal of remote sensing, 41, 3845–3865, 2020.

Mironov, V. L., Kosolapova, L. G., and Fomin, S. V.: Physically and Mineralogically Based Spectroscopic Dielectric Model for Moist Soils, IEEE TRANSACTIONS ON GEOSCIENCE AND REMOTE SENSING, 47, 2059–2070, https://doi.org/10.1109/TGRS.2008.2011631, 2009.

Mironov, V. L., De Roo, R. D., and Savin, I. V.: Temperature-Dependable Microwave Dielectric Model for an Arctic Soil, IEEE Transactions on Geoscience and Remote Sensing, 48, 2544–2556, https://doi.org/10.1109/TGRS.2010.2040034, 2010.

https://doi.org/10.5194/egusphere-2026-2927
Preprint. Discussion started: 31 July 2026

Mironov, V. L., G., K. L., Lukin, Y. I., Y., K. A., and I.P., M.: Temperature- and texture-dependent dielectric model for frozen and thawed mineral soils at a frequency of 1.4 GHz, Remote Sensing of Environment, 200, 240–249, https://doi.org/10.1016/j.rse.2017.08.007, 2017.

Mo, T., Choudhury, B. J., Schmugge, T. J., Wang, J. R., and Jackson, T. J.: A Model For Microwave Emission From Vegetation-Covered Fields, JOURNAL OF GEOPHYSICAL RESEARCH-OCEANS, 87, 1229–1237, https://doi.org/10.1029/JC087iC13p11229, 1982.

Muñoz Sabater, J.: ERA5-Land hourly data from 1950 to present, https://doi.org/10.24381/cds.e2161bac, 2019.

Mätzler, C.: Microwave Permittivity of Dry Snow, IEEE Transactions on Geoscience and Remote Sensing, 34, 573–581, https://doi.org/10.1109/36.485133, 1996.

Mätzler, C. and Schwank, M.: Dielectric properties of heterogeneous media, in: Thermal Microwave Radiation: Applications for Remote Sensing, edited by Mätzler, C., pp. 480–505, The Institution of Electrical Engineers, London, United Kingdom, 2006.

Mätzler, C. and Wiesmann, A.: Extension of the microwave emission model of layered snowpacks to coarse-grained snow, REMOTE SENSING OF ENVIRONMENT, 70, 317–325, https://doi.org/10.1016/S0034-4257(99)00047-4, 1999.

Mätzler, C. and Wiesmann, A.: Documentation for MEMLS, Version 3, 2014.

Mätzler, C., Ellison, W., Thomas, B., Sihvola, A., , and Schwank, M.: Thermal Microwave Radiation: Applications for Remote Sensing, The Institution of Electrical Engineers, London, United Kingdom, https://doi.org/DOI: 10.1049/PBEW052E, 2006.

Naderpour, R., Schwank, M., and Mätzler, C.: Davos-laret remote sensing field laboratory: 2016/2017 winter season L-band measurements data-processing and analysis, Remote Sensing, 9, 1185, 2017.

Naderpour, R., Houtz, D., and Schwank, M.: Snow wetness retrieved from close-range L-band radiometry in the western Greenland ablation zone, Journal of Glaciology, 67, 27–38, 2021.

Njoku, E. G. and Entekhabi, D.: Passive microwave remote sensing of soil moisture, Journal of hydrology, 184, 101–129, 1996.

ONeill, P., Chan, S., Njoku, E., Jackson, T., Bindlish, R., Chaubell, J., and Colliander, A.: SMAP Enhanced L2 Radiometer Half-Orbit 9 km EASE-Grid Soil Moisture, Version 6, https://doi.org/10.5067/BN36FXOMMC4C, 2023.

Ortet, J., Mialon, A., Royer, A., Schwank, M., Holmberg, M., Rautiainen, K., Bircher-Adrot, S., Colliander, A., Kerr, Y., and Roy, A.: Retrieving frozen ground surface temperature under the snowpack in the Arctic permafrost area from SMOS observations, CRYOSPHERE, 19, 3571–3598, https://doi.org/10.5194/tc-19-3571-2025, 2025.

Pellarin, T., Wigneron, J., Calvet, J., Berger, M., Douville, H., Ferrazzoli, P., Kerr, Y., Lopez-Baeza, E., Pulliainen, J., Simmonds, L., and Waldteufel, P.: Two-year global simulation of L-band brightness temperatures over land, IEEE TRANSACTIONS ON GEOSCIENCE AND REMOTE SENSING, 41, 2135–2139, https://doi.org/10.1109/TGRS.2003.815417, 2003.

Peplinski, N. R., Ulaby, F. T., and Dobson, M. C.: Dielectric-Properties of Soils in the 0.3-1.3-Ghz Range, IEEE TRANSACTIONS ON GEOSCIENCE AND REMOTE SENSING, 33, 803–807, https://doi.org/10.1109/36.387598, 1995.

Picard, G., Sandells, M., and Loewe, H.: SMRT: an active-passive microwave radiative transfer model for snow with multiple microstructure and scattering formulations (v1.0), GEOSCIENTIFIC MODEL DEVELOPMENT, 11, 2763–2788, https://doi.org/10.5194/gmd-11-2763-2018, 2018.

Piles, M., Entekhabi, D., and Camps, A.: A change detection algorithm for retrieving high-resolution soil moisture from SMAP radar and radiometer observations, IEEE Transactions on Geoscience and Remote Sensing, 47, 4125–4131, 2009.

Rautiainen, K., Parkkinen, T., Lemmetyinen, J., Schwank, M., Wiesmann, A., Ikonen, J., Derksen, C., Davydov, S., Davydova, A., Boike, J., Langer, M., Drusch, M., and Pulliainen, J.: SMOS Prototype Algorithm for Detecting Autumn Soil Freezing, Remote Sensing of Environment, 180, 346–360, https://doi.org/10.1016/j.rse.2016.01.012, 2016.

https://doi.org/10.5194/egusphere-2026-2927
Preprint. Discussion started: 31 July 2026

Reichle, R. H., Lannoy, G. J. M. D., Liu, Q., Ardizzone, J. V., Colliander, A., Conaty, A., Crow, W., Jackson, T. J., Jones, L. A., Kimball, J. S., Koster, R. D., Mahanama, S. P., Smith, E. B., Berg, A., Bircher, S., Bosch, D., Caldwell, T. G., Cosh, M., Ángel González-Zamora, Collins, C. D. H., Jensen, K. H., Livingston, S., Lopez-Baeza, E., Martínez-Fernández, J., McNairn, H., Moghaddam, M., Pacheco, A., Pellarin, T., Prueger, J., Rowlandson, T., Seyfried, M., Starks, P., Su, Z., Thibeault, M., van der Velde, R., Walker, J., Wu, X., and Zeng, Y.: Assessment of the SMAP Level-4 Surface and Root-Zone Soil Moisture Product Using In Situ Measurements, Journal of Hydrometeorology, 18, 2621–2645, https://doi.org/10.1175/JHM-D-17-0063.1, 2017.

Reul, N., Grodsky, S., Arias, M., Boutin, J., Catany, R., Chapron, B., d'Amico, F., Dinnat, E., Donlon, C., Fore, A., et al.: Sea surface salinity estimates from spaceborne L-band radiometers: An overview of the first decade of observation (2010–2019), Remote Sensing of Environment, 242, 111 769, 2020.

Rodriguez-Fernandez, N. J., Aires, F., Richaume, P., Kerr, Y. H., Prigent, C., Kolassa, J., Cabot, F., Jimenez, C., Mahmoodi, A., and Drusch, M.: Soil moisture retrieval using neural networks: Application to SMOS, IEEE Transactions on Geoscience and Remote Sensing, 53, 5991–6007, 2015.

Rodriguez-Fernandez, N. J., Mialon, A., Mermoz, S., Bouyet, A., Richaume, P., Al Bitar, A., Al-Yaari, A., Brandt, M., Kaminski, T., Toan, T. L., Kerr, Y. H., and Wigneron, J.-P.: An evaluation of SMOS L-band vegetation optical depth (L-VOD) data sets: high sensitivity of L-VOD to above-ground biomass in Africa, BIOGEOSCIENCES, 15, 4627–4645, https://doi.org/10.5194/bg-15-4627-2018, 2018.

Rodríguez-Fernández, N., de Rosnay, P., Albergel, C., Richaume, P., Aires, F., Prigent, C., and Kerr, Y.: SMOS Neural Network Soil Moisture Data Assimilation in a Land Surface Model and Atmospheric Impact, Remote Sensing, 11, 1334, https://doi.org/10.3390/rs11111334, 2019.

Santamarina, J. C., Klein, A., and Fam, M. A.: Soils and waves: Particulate materials behavior, characterization and process monitoring, Journal of Soils and Sediments, 1, 130–130, 2001.

Schwank, M., Rautiainen, K., Maetzler, C., Staehli, M., Lemmetyinen, J., Pulliainen, J., Vehvilainen, J., Kontu, A., Ikonen, J., Menard, C., Drusch, M., Wiesmann, A., and Wegmueller, U.: Model for Microwave Emission of a Snow-Covered Ground With Focus on L Band, Remote Sensing of Environment, 154, 180–191, https://doi.org/10.1016/j.rse.2014.08.029, 2014.

Schwank, M., Maetzler, C., Wiesmann, A., Wegmueller, U., Pulliainen, J., Lemmetyinen, J., Rautiainen, K., Derksen, C., Toose, P., and Drusch, M.: Snow Density and Ground Permittivity Retrieved from L-Band Radiometry: A Synthetic Analysis, IEEE JOURNAL OF SELECTED TOPICS IN APPLIED EARTH OBSERVATIONS AND REMOTE SENSING, 8, 3833–3845, https://doi.org/10.1109/JSTARS.2015.2422998, 2015.

Schwank, M., Naderpour, R., and Mätzler, C.: "Tau-Omega"- and Two-Stream Emission Models Used for Passive L-Band Retrievals: Application to Close-Range Measurements Over a Forest, Remote Sensing, 10, https://doi.org/10.3390/rs10121868, 2018.

Schwank, M., Kontu, A., Mialon, A., Naderpour, R., Houtz, D., Lemmetyinen, J., Rautiainen, K., Li, Q., Richaume, P., Kerr, Y., and Maetzler, C.: Temperature Effects on L-Band Vegetation Optical Depth of a Boreal Forest, Remote Sensing of Environment, 263, https://doi.org/10.1016/j.rse.2021.112542, 2021.

Schwank, M., Zhou, Y., Mialon, A., Richaume, P., Kerr, Y., and Matzler, C.: Temperature dependence of L-band vegetation optical depth over the boreal forest from 2011 to 2022, REMOTE SENSING OF ENVIRONMENT, 315, https://doi.org/10.1016/j.rse.2024.114470, 2024.

Sihvola, A. H. and Kong, J. A.: Effective permittivity of dielectric mixtures, IEEE Transactions on Geoscience and Remote Sensing, 26, 420–429, 2002.

Tsang, L., Kong, J. A., and Ding, K.-H.: Scattering of Electromagnetic Waves: Theories and Applications, Wiley–Interscience, New York, 2000.

https://doi.org/10.5194/egusphere-2026-2927
Preprint. Discussion started: 31 July 2026

Ulaby, F. T., Moore, R. K., and Fung, A. K.: Microwave remote sensing: Active and passive. volume 1-microwave remote sensing fundamentals and radiometry, Microwave remote sensing: Active and passive. Volume 1-Microwave remote sensing fundamentals and radiometry by Ulaby, 1, 39 342, 1981.

Urban, F. and Clow, G.: DOI/GTN-P climate and active-layer data acquired in the National Petroleum Reserve–Alaska and the Arctic National Wildlife Refuge, 1998–2019, U.S. Geological Survey Data Series 1092, https://doi.org/https://doi.org/10.3133/ds1092.

Vittucci, C., Laurin, G. V., Tramontana, G., Ferrazzoli, P., Guerriero, L., and Papale, D.: Vegetation optical depth at L-band and above ground biomass in the tropical range: Evaluating their relationships at continental and regional scales, INTERNATIONAL JOURNAL OF APPLIED EARTH OBSERVATION AND GEOINFORMATION, 77, 151–161, https://doi.org/10.1016/j.jag.2019.01.006, 2019.

Wang, J. and Choudhury, B.: Remote Sensing of Soil Moisture Content Over Base Field at 1.4GHz Frequency, Journal of Geophysical Research, 86, 5277–5282, https://doi.org/10.1029/JC086iC06p05277, 1981.

Wiesmann, A. and Mätzler, C.: Microwave Emission Model of Layered Snowpacks, Remote Sensing of Environment, 70, 307–316, https://doi.org/10.1016/S0034-4257(99)00046-2, 1999.

Wigneron, J.-P., Kerr, Y., Waldteufel, P., Saleh, K., Escorihuela, M.-J., Richaume, P., Ferrazzoli, P., de Rosnay, P., Gurney, R., Calvet, J.-C., Grant, J. P., Guglielmetti, M., Hornbuckle, B., Maetzler, C., Pellarin, T., and Schwank, M.: L-band Microwave Emission of the Biosphere (L-MEB) Model:: Description and calibration against experimental data sets over crop fields, REMOTE SENSING OF ENVIRONMENT, 107, 639–655, https://doi.org/10.1016/j.rse.2006.10.014, 2007.

Wilson, R. W.: The cosmic microwave background radiation, Science, 31, 866–874, 1979.

Wohlfahrt, G., Sapinsky, S., Tappeiner, U., and Cernusca, A.: Estimation of plant area index of grasslands from measurements of canopy radiation profiles, Agricultural and Forest Meteorology, 109, 1–12, 2001.

World Meteorological Organization (WMO) et al.: Implementation Plan for the Global Observing System for Climate in Support of the UNFCCC (2010 Update), GCOS Report GCOS-138, WMO, Geneva, Switzerland, 2022.

Wu, X.: Implementation of two-stream emission model for L-band retrievals on the Tibetan Plateau, Remote Sensing, 14, 494, 2022.

Zhou, Y. and et al.: Satellite Microwave Radiometry at L-band for Monitoring Earth's Essential Climate Variables, in review, 2026.

Zhou, Y., Schwank, M., Kurum, M., Houtz, D., Zhao, Q., Lang, R., Mialon, A., and Drusch, M.: Microwave Emission Model for Layered Vegetation (MEMLV): An Exemplary Study for Coniferous Forests From P- to Ka-Band, IEEE Transactions on Geoscience and Remote Sensing, 62, https://doi.org/10.1109/TGRS.2024.3491218, 2024.

Zotta, R.-M., Moesinger, L., Van Der Schalie, R., Vreugdenhil, M., Preimesberger, W., Frederikse, T., De Jeu, R., and Dorigo, W.: VODCA v2: Multi-sensor, multi-frequency vegetation optical depth data for long-term canopy dynamics and biomass monitoring, Earth System Science Data, 16, 4573–4617, 2024.